



1-1-2018

Molecular Dynamics Simulation Of Gas Transport And Adsorption In Ultra-Tight Formations

Yannick Tambe Agbor

Follow this and additional works at: <https://commons.und.edu/theses>

 Part of the [Engineering Commons](#)

Recommended Citation

Agbor, Yannick Tambe, "Molecular Dynamics Simulation Of Gas Transport And Adsorption In Ultra-Tight Formations" (2018).
Theses and Dissertations. 2098.

<https://commons.und.edu/theses/2098>

This Thesis is brought to you for free and open access by the Theses, Dissertations, and Senior Projects at UND Scholarly Commons. It has been accepted for inclusion in Theses and Dissertations by an authorized administrator of UND Scholarly Commons. For more information, please contact zeinebyousif@library.und.edu.

MOLECULAR DYNAMICS SIMULATION OF GAS TRANSPORT AND ADSORPTION IN
ULTRA-TIGHT FORMATIONS

By

Yannick Tambe Agbor

Bachelor of Science, University of Buea, 2013

Master of Science, Khazar University, 2016

A Thesis

Submitted to the Graduate Faculty

Of the

University of North Dakota

In partial fulfillment of the requirements

For the degree of

Master of Science

Grand Forks, North Dakota

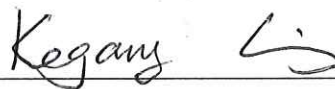
December

2018

This thesis, submitted by Yannick Tambe Agbor in partial fulfillment of the requirements for the Degree of Master of Science from the University of North Dakota, has been read by the Faculty Advisory Committee under whom the work has been done and is hereby approved.



Chairperson (Hui Pu)



Committee Member (Kegang Ling)



Committee Member (Bailey Bubach)

This thesis is being submitted by the appointed advisory committee as having met all of the requirements of the School of Graduate Studies at the University of North Dakota and is hereby approved.



Grant McGimpsey

Dean of the School of Graduate Studies



Date

PERMISSION

Title	Molecular Dynamics Simulation of Gas Transport and Adsorption in Ultra-Tight Formations
Department	Petroleum Engineering
Degree	Master of Science

In presenting this thesis in partial fulfillment of the requirements for a graduate degree from the University of North Dakota, I agree that the library of this University shall make it freely available for inspection. I further agree that permission for extensive copying for scholarly purposes may be granted by the professor who supervised my thesis work or, in his absence, by the Chairperson of the department or the dean of the School of Graduate Studies. It is understood that any copying or publication or other use of this thesis or part thereof for financial gain shall not be allowed without my written permission. It is also understood that due recognition shall be given to me and to the University of North Dakota in any scholarly use which may be made of any material in my thesis.

Yannick Tambe Agbor

11/17/2018

TABLE OF CONTENTS

LIST OF FIGURES	vi
ACKNOWLEDGEMENTS.....	viii
ABSTRACT.....	x
CHAPTER ONE :INTRODUCTION.....	1
1.1. Organic Content Estimation.....	3
1.2. Adsorption in shales.....	9
1.3 Transport in Shales.....	11
CHAPTER TWO :INTRODUCTION TO MOLECULAR SIMULATION.....	14
2.1 Molecular Dynamics	14
2.1.1) Force Fields.....	15
2.1.2) Energy Minimization.....	17
2.1.3) Non Bonded Interactions and Long Range Electrostatics.....	19
2.1.4) Equilibration.....	22
2.1.5) Temperature Coupling.....	23
2.1.6) Intergrators	27
2.2) Monte Carlo Simulations	28
CHAPTER THREE: GAS TRANSPORT IN SHALE NANOPORES AND PORE NETWORK MODELLING	31
3.1 Gas Transport in Kerogen	31
3.2 Microscale Pore Network Modelling	35
3.3. Model and Methods.....	36
3.3.1 Kerogen Molecular Model.....	36
3.3.2 Porosity Characterization	38
3.3.3 Diffusion Coefficient.....	38
3.4. Pore Network Model Construction	40
3.5 Results And Discussions	43

3.5.1 Methane and Ethane Transport Diffusivity	43
3.5.2. Porosity And MICP	46
3.6. Conclusions	48
CHAPTER FOUR: MOLECULAR SIMULATION OF METHANE, ETHANE AND CARBONDIOXIDE ADSORPTION IN SHALE GAS SYSTEMS	49
4.1 Simulation Details	56
4.2 Results	60
4.2.1. Adsorption of Methane and CO ₂ in Kerogen Nanopores	60
4.2.2 Adsorption Of Methane, Ethane and CO ₂ In Silica and Organic Pore Channel	64
4.3. Conclusion.....	67
References	68

LIST OF FIGURES

Figure 1.1	Focused Ion Beam - Scanning Electron Microscopy (<i>FIB-SEM</i>) on Gas Shale sample	2
Figure 1.2	Gas distribution in gas shale samples from the Barnett formation	2
Figure 1.3	Young modulus vs shale TOC	3
Figure 1.4	Raman spectra (intensity versus Raman shift) for 5 samples from the Bakken	4
Figure 1.5	Raman shift for 5 samples from the Bakken	6
Figure 1.6	Band separation and vitrinite reflectance for different shale formations	7
Figure 1.7	Transmission electronic microscopy (TEM) image of three samples with different maturities	8
Figure 1.8	Kerogen Quality	9
Figure 1.9	Excess adsorption isotherms of methane	10
Figure 1.10	Pore size distribution, determined by Clarkson et al., on a gas shale sample from the Barnett formation.	11
Figure 1.11	Square root time vs. total gas content. Blue dots represents measured gas volume in canister can experiment for one sample	13
Figure 2.1	Schematic diagram of the various bonded interactions. a) Bond stretching b) bond angle bending and c) dihedral rotation.	17
Figure 2.2	Graph illustrating steps in energy minimization	18
Figure 2.3	Leap Frog integration method	30
Figure 2.4	Translation move: Random displacement of a particle within the box	31
Figure 2.5	Change of volume MC move.	32
Figure 3.1	Flow regimes	34
Figure 3.3	Kerogen nanopores	35

Figure 3.4	Molecular structure of type II kerogen.	39
Figure 3.5	Final structure of the eighteen kerogen units placed in a simulation box to form nanopores matrix	40
Figure 3.6	Pore network model created using the Delaunay triangulation	43
Figure 3.7	Pore network model showing the distribution of the pore spaces.	43
Figure 3.8	Pore connectivity by the Delaunay triangulation method.	44
Figure 3.9	Pore and throat size distribution for created model	45
Figure 3.10	Ethane flow in kerogen after 2ns	46
Figure 3.11	Methane diffusion coefficients vs. pressure	47
Figure 3.12	Ethane diffusion coefficients vs. pressure	47
Figure 3.13	Methane and Ethane diffusion coefficients vs. pressure	48
Figure 3.14	Porosity calculation in xyz directions	49
Figure 3.15	Capillary pressure curve vs saturation for invading and defending phases	49
Figure 4.1	Gas Distribution in Shale Formations	52
Figure 4.2	SEM image of a kerogen body showing porosity	53
Figure 4.3	BSE image from nine different shale plays	53
Figure 4.4	Type II Kerogen structure used for simulation	59
Figure 4.5	Initial model of methane molecules in 4.5nm silica pore channel	60
Figure 4.6	Initial model of ethane molecules in a 5nm carbon channel	60
Figure 4.7	Absolute adsorption of CO ₂ and CH ₄ in kerogen	64
Figure 4.8	Excess adsorption of CO ₂ and CH ₄ in kerogen	65
Figure 4.9	Density of adsorbed fluids in kerogen	65
Figure 4.10	Methane and ethane adsorption in Silica nanopores channel	66

ACKNOWLEDGEMENTS

I wish to express my sincere appreciation to the members of my advisory
Committee: Dr Hui Pu, Dr Kegang Ling and Bailey Bubach for their guidance and support
during my time in the master's program at the
University of North Dakota.

This work is dedicated to God Almighty. To my late dad Martin and my mom Martha, the best people I have ever known.

ABSTRACT

Kerogen, which plays a very important part in reservoir characterization for ultra-tight formations, is also involved in the storage and production of hydrocarbons in shale. In this work, we study the kerogen structure and its interaction with insitu hydrocarbons to fully understand the fluid flow and adsorption mechanisms in the shale. Also the advancement in pore network modelling has greatly helped the understanding of mesoscale fluid flow. In this work, transport of methane in a type II marine environment kerogen model is studied using molecular dynamics simulations. Non Equilibrium Molecular Dynamics Simulations (NEMDS) using GROMACS code and Grand Canonical Monte Carlo (GCMC) using the RASPA code have been applied to simulate the adsorption and transport of ethane, carbon dioxide and methane in nanoscale environment. In this work, we used the kerogen and silica pore models to represent an organic and inorganic nanopore channels, respectively. The initial configuration models are then energy minimized, and both constant-temperature constant-volume (NVT) simulations and then constant-temperature constant-pressure (NPT) simulations are performed to obtain the final structure.

For our pore network model, we used the Delaunay triangulation method to build a network model and then employed capillary pressure simulations. The simulation results from molecular simulations transport diffusivities show that as pressure increases the transport diffusion coefficients increase. Methane has a higher diffusivity in kerogen than ethane at the same temperature and pressure conditions.

For adsorption, results show that CO₂ has the largest adsorption capacity for both organic and inorganic pores, hence, a good candidate for enhanced gas recovery and carbon sequestration in depleted shale gas reservoirs. The amount of adsorption is more in organic pores for all studied gases, which implies that shale reservoirs with higher total organic carbon (TOC) will turn to trap more gases restricting flow and production.

CHAPTER ONE

INTRODUCTION

Over the recent years, global oil demand has forced companies and countries to exploit even reserves that were deemed uneconomical in the early 2000's. Unconventional reservoirs are being currently aggressively developed in North America with recent breakthrough in new technologies such as multi-stage fractured horizontal wells. Recent advancements in horizontal drilling and hydraulic fracturing have significantly increased the oil production from unconventional shale reservoirs such as the Bakken, Eagle Ford, and Barnett Formations. Shale in the oil and gas industry can be different as two kinds of resources; shale gas/oil and oil shales. They correspond to very shallow fine grain sedimentary rocks rich in organic matter. Due to the shallow burial depth, the pressure and temperature conditions did not allow the cracking of the organic matter into gas and oil. Shale gas or oil refers to oil and gas trapped in rocks of extremely low permeability. The permeability in those reservoir rocks range from nano-Darcy to hundreds of micro-Darcy. When looking at a shale sample at the microscale, nodules of organic matter is scattered within an inorganic matrix. This organic matter is dominantly kerogen, while the inorganic matrix is mostly quartz, calcite and clay minerals. Fig 1.1 shows the presence of kerogen nanopores in a clay matrix(Ma et al., 2014). These pore spaces contain adsorbed gas bound to the pore walls by electrostatic forces of attraction.

Shales and tight reservoirs differ from conventional reservoirs because of the nature of fluid flow, storage and location of their hydrocarbon content. Most of the hydrocarbons in tight reservoirs are adsorbed and the rest appear as free gas. Fig 1.2 shows the amount of free and

adsorbed gas in typical Barnett shale samples, and from the analysis only a third of the total gas is found in the inorganic phase (Ma et al., 2014).

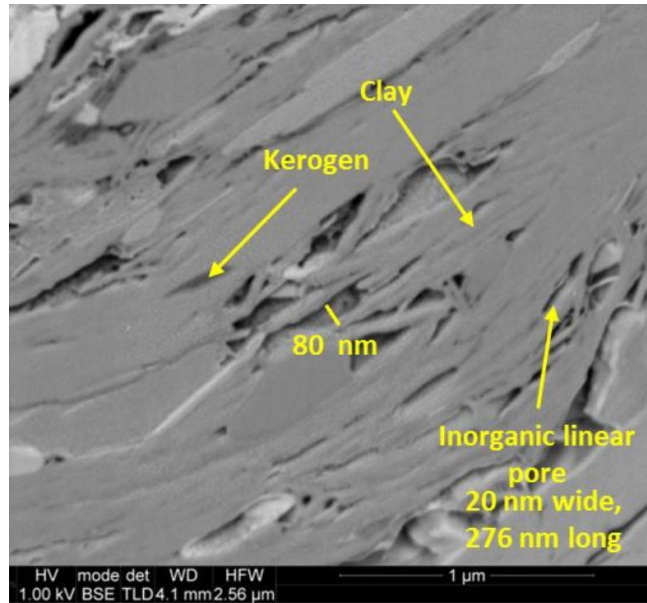


Fig 1.1: Focused Ion Beam - Scanning Electron Microscopy (*FIB-SEM*) on Gas Shale sample (Ma et al., 2014)

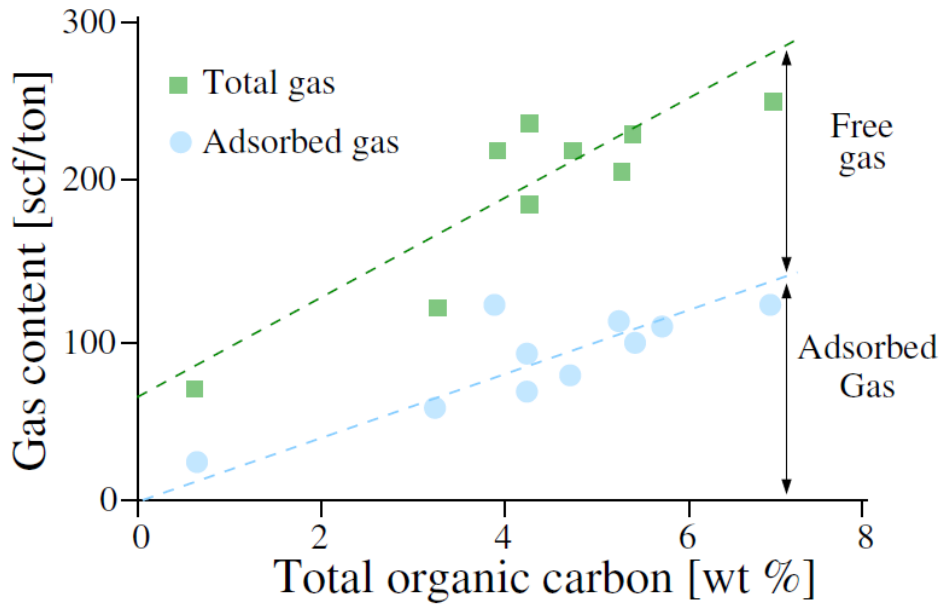


Fig 1.2: Gas distribution in gas shale samples from the Barnett formation (Ma et al., 2014)

1.1. Organic Content Estimation

Despite the extensive study of the presence of organic matter in shale rocks, kerogen which is the major constituent of the rock's organic matter is still ill understood. This organic matter, predominantly kerogen, is being formed from the burial and preservation of living organisms, and then interspersed within the mineral matrix (Hulton et al., 1994). The amount of kerogen in shale can affect the rock's mechanical properties; shales with higher TOC will tend to have lower fracture pressure gradients which imply that kerogen has considerable effect on the rock mechanical response (Fig 1.3) (Kumar et al., 2012).

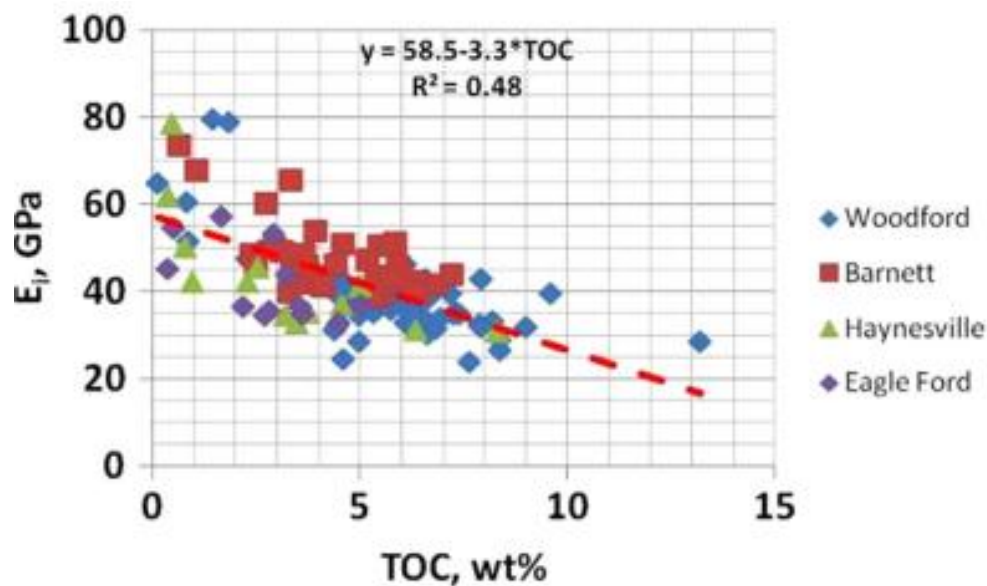


Fig 1.3: Young modulus vs shale TOC (Kumar et al, 2012)

Organic matter experiences increase in aromaticity and H, O, N and S reduction during maturation. This results in a more ordered-structure which makes it feasible to use Raman spectroscopy to detect different levels of thermal maturation, reflecting any structural changes.

TOC can be measured in three main ways; Rock-Eval (RE) method (Espitalie et al., 1985; Peters, 1986), Vitrinite Reflectance (%VRO) method and Raman Spectroscopy.

Rock-Eval (RE) pyrolysis has been used widely to characterize organic matter type, thermal maturity and source rock potential for organic-rich rocks. TOC can be determined using the RE method. There are three main types of Rock-Eval method: the default method, reservoir method and shale reservoir method. The shale reservoir method is widely used for shale reservoirs and involves putting a sample in a pyrolysis chamber with initial temperature of 100°C. The temperature is then increased to 200°C at 25°C/min and held constant for 3 min, then increased to 350°C at 25°C/min and finally to 650°C at 25°C/min.

Raman Spectroscopy has also been used recently to determine the thermal maturity level for organic-shale rocks. Raman scattering is a function of the molecular vibrations which can produce a Raman shift. This method is more accurate than Rock-Eval and VRO because their rock is not crushed, meaning all the faces of the rock are preserved with no form of distortion.

The Raman spectrum of kerogen consists of two main peaks called the G and D bands (Tuschel, 2013). The G refers to graphite, which generally appears around $1,600\text{cm}^{-1}$ as a very sharp peak (Fig 1.4). The origin of the G band is mainly due to the inplane vibrational modes of the carbon atoms in the aromatic ring structures. The D band, which refers to disorder in the atoms, has a peak around $1,350\text{cm}^{-1}$ as a narrow peak which is associated with defects in the lattice structure and discontinuities of the carbon network. Generally, during the process of thermal maturation, kerogen endures aromaticity and turns to be more ordered which leads to the disappearance of the disorder band, D. Meanwhile, for poorly organized organic matter, additional bands maybe appear at around $1,150$, $1,350$, $1,500$ and $1,620\text{cm}^{-1}$.

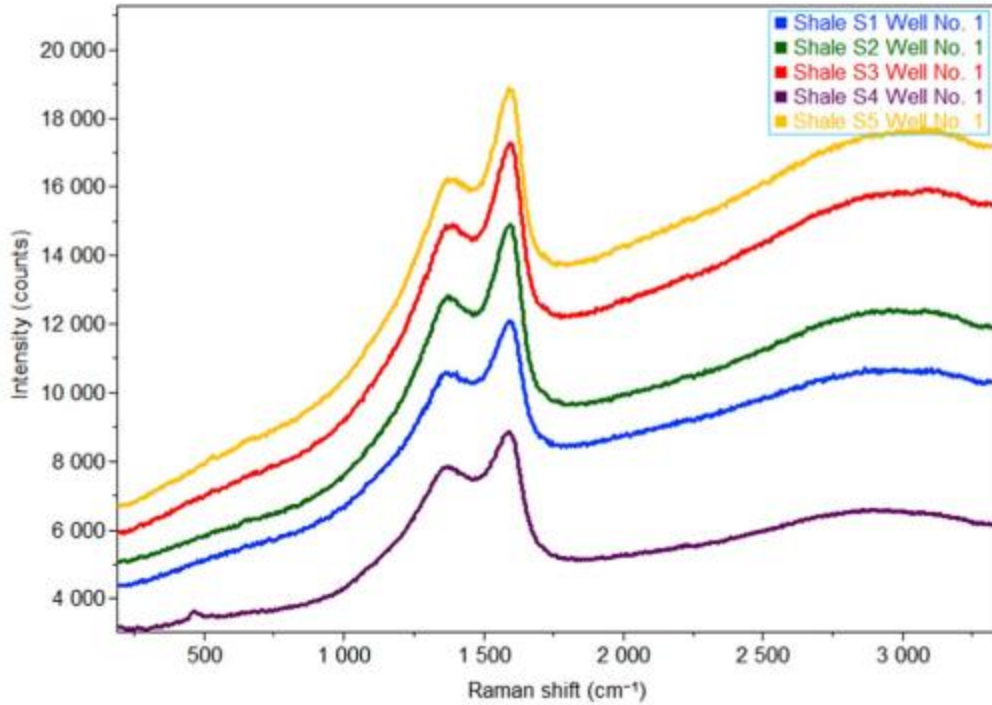


Fig 1.4: Raman spectra (intensity versus Raman shift) for 5 samples from the Bakken (Khatibi et al, 2017)

Khatibi et al (2017) found out that the Raman response shows a trend between the depth of the sample and the band position. The D band position turn to shift to the left ($1,367$ to $1,354 \text{ cm}^{-1}$) as the depth increases which can be attributed to increase in thermal maturity (Fig 1.5). This shift of the D band to lower wavelengths would signify an increase of larger aromatic clusters and a more ordered-structure kerogen. Also, taking the band separation distance (G-D) and correlating with vitrinite reflectance ($\%R_o$), there is a non-linear relationship with G-D distance increasing as the R_o increases (Fig 1.6). At initial stages of maturation, band separation increases with a higher intensity while this rapid growth tapers off over higher maturities.

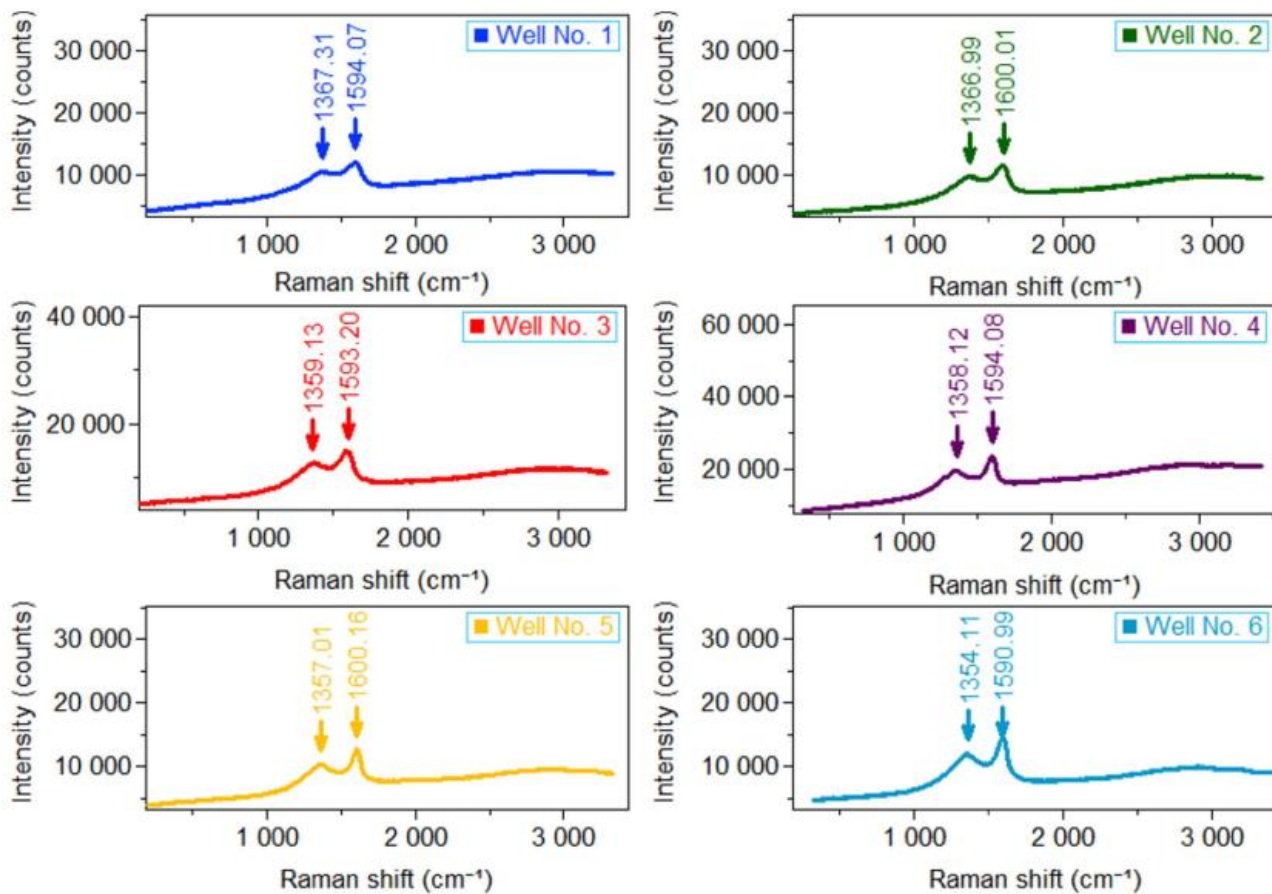


Fig 1.5: Raman shift for 5 samples from the Bakken. (Source: Khatibi et al., 2017)

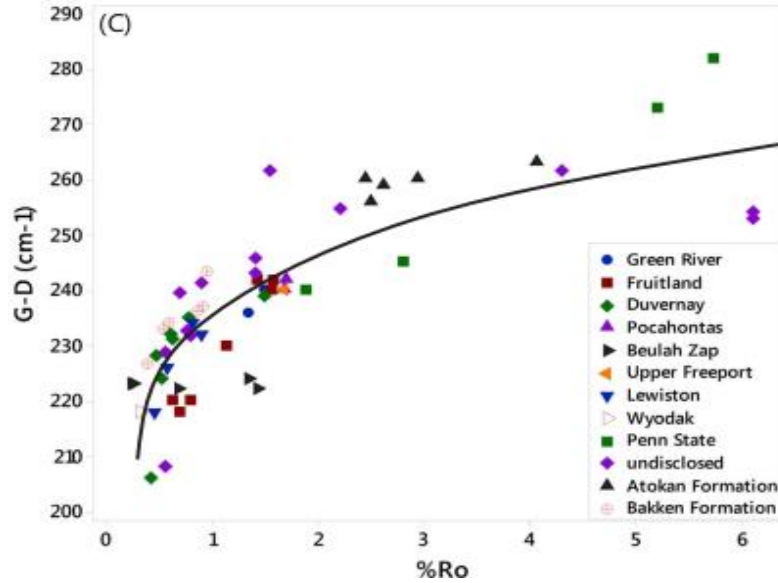


Fig 1.6: Band separation and vitrinite reflectance for different shale formations (Khatibi et al., 2017)

From a molecular point of view, when maturity happens, kerogen loses heteroatoms (N, S, and O) and its aliphatic carbons (hydrogen-rich groups). The residue is a hydrogen-poor structure molecule, which is dominated by aromatic carbons. During the process of maturation, which increases with burial depth, pore-walls rupture. This sequence promotes the mechanical reorientation and alignment of the aromatic units, thus will facilitate the reduction of defects. This is due to diffusion, elimination of bonding vacancies and annealing of aromatic sheets to triperiodic graphite (Bustin,1996). Therefore, from the early stages of maturation, the macromolecule arrangements transform gradually from the chaotic and mixed layers to a more ordered arrangement (Pan et al., 2013). Fig 1.7 shows molecular arrangement of some samples under high-resolution transmission electronic microscope (TEM). TEM showed, in the samples with lower maturity, layers are stacked together in groups of two or three with length < 1 nm. While, in the more mature samples, not only the number of stacked layers slightly increases but also the length of distorted layers reaches 4 nm (Quirico et al., 2005). As a result, there is a

significant change in the molecular structure of kerogen as the thermal maturity increases (Emmanuel et al., 2016).

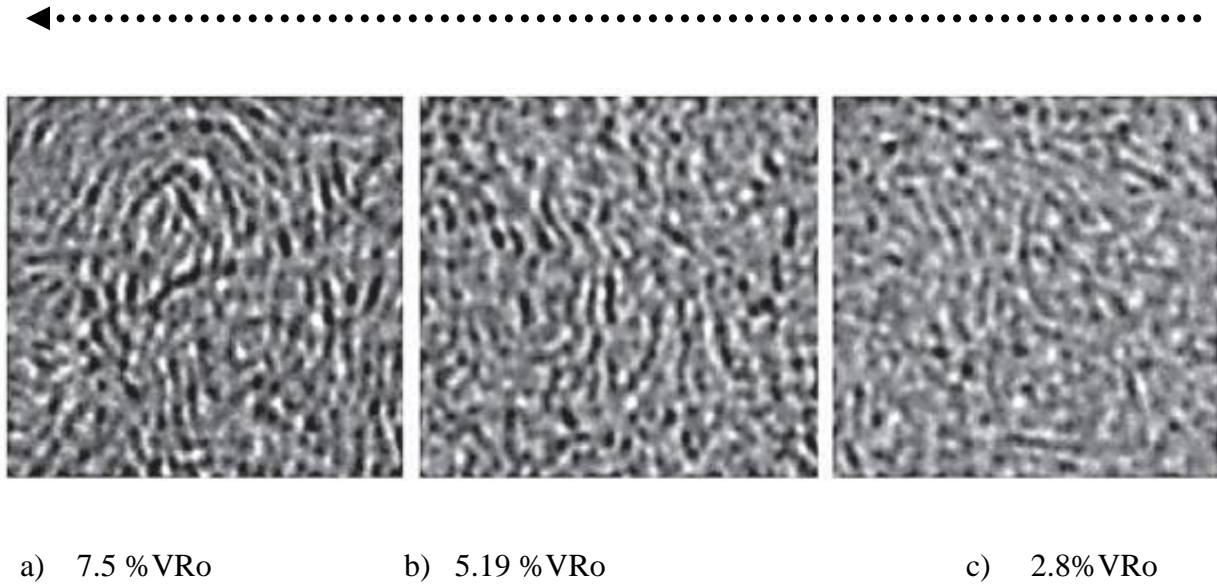


Fig 1.7: Transmission electronic microscopy (TEM) image of three samples with different maturities. (Source: Quirico et al., 2005)

Vitrinite reflectance (VRo) analysis is based on the reflectance of UV light when focusing on the sample. The sample to be tested is crushed to fine particles to about 20 meshes, mixed with epoxy resin and hardener, left to harden under vacuum for about 24hrs (Hackley et al., 2015). The samples are polished and placed in the testing cell which is equipped with white light and UV light to analyze the reflectance. Khatabi et al (2017) and Liu et al (2017) conducted detailed work using VRo analysis to determine the TOC of the Lower and Upper Bakken Formations. They both found out that VRo is lesser for rocks with higher TOC, and hence the Middle Bakken member had the highest VRo values.

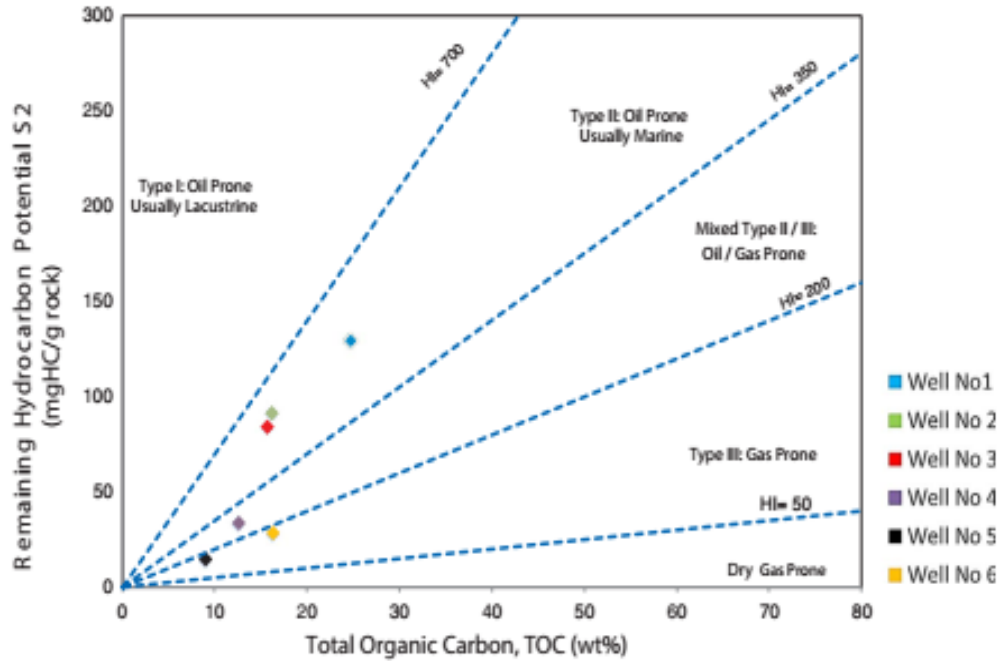


Fig 1.8: Kerogen Quality (Khatabi et al., 2017)

1.2. Adsorption in shales

Adsorption experiments have been performed to estimate the storage properties of shale samples. The reasons for these experiments is to predict reserves at a given reservoir pressure and the quantity of fluids that can be recovered. The composition of the adsorbed phase, which is generally richer in hydrocarbons than the free phase can be correctly predicted from adsorption experiments.

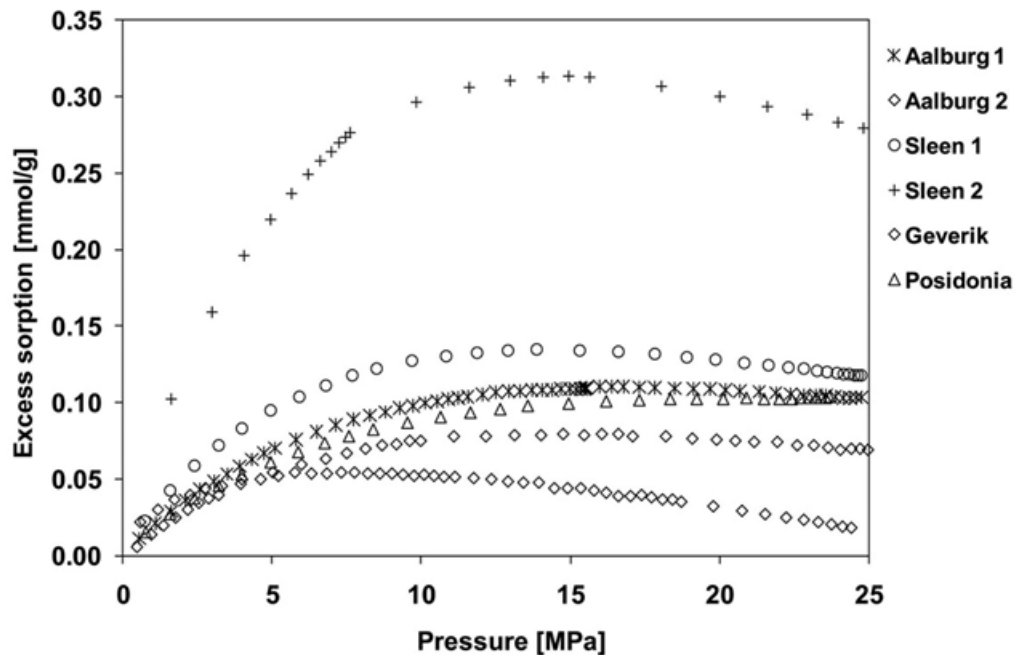


Fig 1.9. Excess adsorption isotherms of methane at 65°C (from Gasparik et al., 2014 on shale samples from the Netherlands.)

Quantitatively, shales have a maximum excess adsorption amount of few millimoles per gram of the Total Organic Carbon (TOC). This amount is one order of magnitude lower than the maximum adsorption in coals and twice lesser in magnitude as in activated carbon.

Fig 1.9 shows the methane excess adsorption isotherms performed by Gasparik et al (2014). As seen in Fig 1.9 the properties and content of organic matter in sedimentary rocks can differ considerably from sample to sample and this is mainly due to the type and history of the diagenetic processes (burial and sedimentation). However, there are so many limitations in trying to investigate adsorption in shales experimentally. Firstly, it is fairly impossible to completely dry the samples because the residual water will create capillary bridges which will prevent gas in the pores of the organic matter, hence introducing a strong bias to the results obtained. The experimental results reported in Fig 1.9 have been investigated by 7 different

laboratories and the discrepancy in their results scale up to 50%. And secondly, experimental adsorption isotherms have been determined mainly on supercritical methane, ethane or carbon dioxide under a range of reservoir temperature (300 – 450K). This is little or no experimental work on richer and less mature resources to produce data for adsorption isotherm and hence a complete adsorption model for shales.

1.3 Transport in Shales

The use of imaging techniques such as *FIB-SEM* and CT- Scanning has greatly given more light into the existence of nearly spherical pores less than 20 nm in diameter. With these imaging techniques, micro-pores with width smaller than 2nm has been confirmed. These micropores represent a non-negligible fraction of the porous volume and porous surface, as shown in Fig

1.10

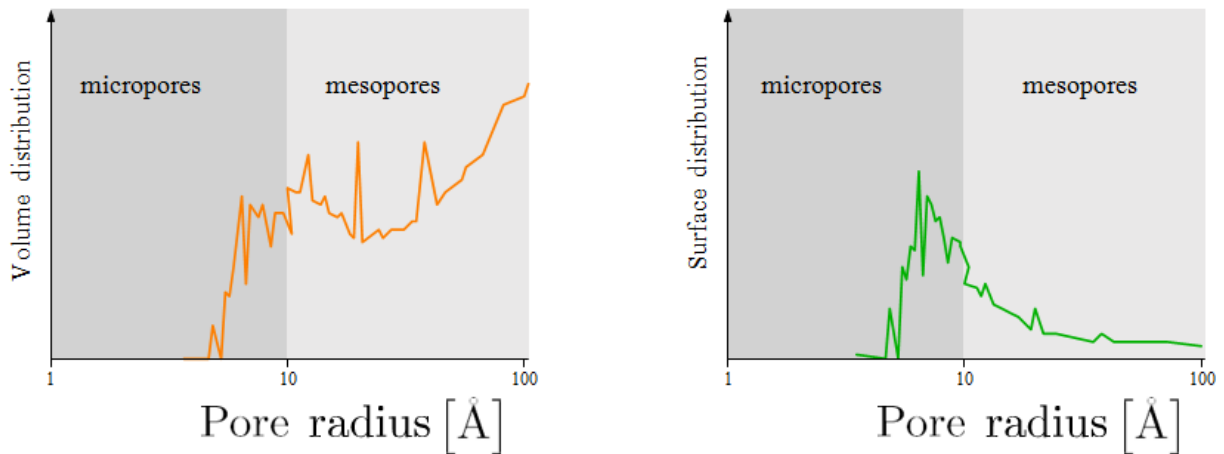


Fig. 1.10: Pore size distribution, determined by Clarkson et al., 2012, on a gas shale sample from the Barnett formation.

It is reported by some researchers that these pores originate from the cracking of liquid hydrocarbons into dry gas along the gas formation window, which then expands forming bubbles

inside the matrix of the organic matter. Due to the shale gas revolution so many studies both experimental and molecular simulations have been performed to predict the diffusion of gas and liquid hydrocarbons in shales. The experimental work done by Thomas et al (1990) on the diffusion of liquid hydrocarbon in shales found that the effective diffusivities were around 10^{-14} m²/s. This was later confirmed for methane diffusion in shale by the use of molecular dynamic simulations.

NMR experiments as well as molecular simulations in carbon nanopores report self-diffusion coefficients for oil of 10^{-9} m²/s in the organic matter.

There is always a question as to whether diffusion process has significant effect at a reservoir scale. From core experiments and history production data that the mass transfer of gas in intact (unfractured) shales is mainly due to diffusion mechanisms, with possible molecular sieving effects during recovery. Thus, the diffusion process, which is intimately related to the transport process at the small scale, is still relevant at the macroscale.

Pujol et al(2013) focused on the explanation of canister can experiments. These experiments are used in the oil and gas industry to estimate the gas in place under reservoir conditions in a core sample. They consist in measuring the rate and quantities of expelled gas from a core sample at atmospheric pressure and ambient temperature.

However, the extraction of the core samples used in canister can experiments is performed in open-air conditions. Thus, a non negligible hydrocarbon amount is lost during this step. An example of such experiments is given in Fig 1.11. The first experimental point, corresponding to the yellow square, has been determined 9 hours after the extraction of the core sample. The volume of lost gas during this time period, required to calculate the total gas content is

determined from a linear extrapolation of the first six experimental points, which implicitly assumes that the flows can be described using a Darcy like law, as shown in Fig 1.11.

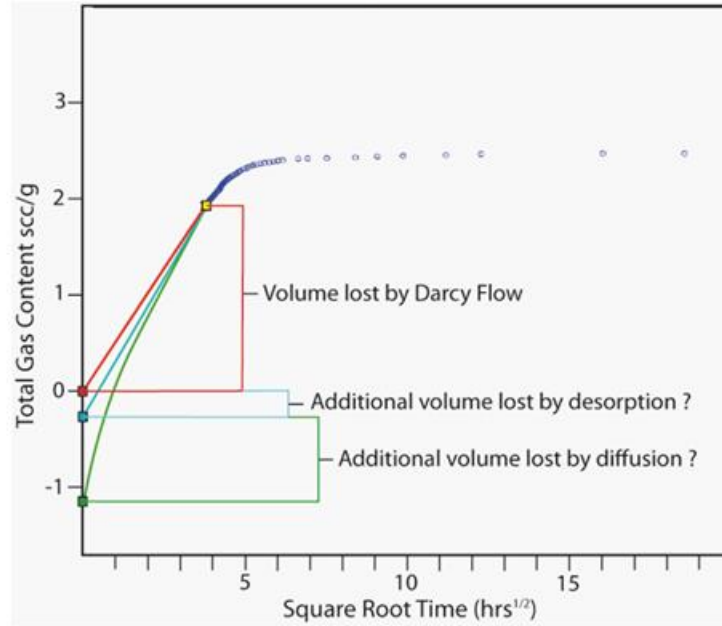


Fig. 1.11: Square root time vs. total gas content. Blue dots represents measured gas volume in canister can experiment for one sample. (Pujol et al., 2013)

Furthermore, Pujol et al (2013) combined molecular simulations with experimental results on the molecular and isotopic compositions of the gas steam. It has been shown that in order to fit the isotopic gas phase evolution, molecular diffusion has to be taken into account. In addition, it was shown a strong correlation between desorption and diffusion, suggesting that the diffusing gases were adsorbed in the organic matter. For the shales gas samples studied, up to 40 % of the total gas can be produced by these non Darcean process, indicating a strong impact of the nanoscale even at the macroscale. Thus, there is a need to deeper characterize adsorption and transport processes in shales organic matter, as this will impact the whole recovery process.

CHAPTER TWO INTRODUCTION TO MOLECULAR SIMULATIONS

2.1 Molecular Dynamics

As discussed in the previous chapter, molecular dynamic simulations help in understanding molecules in terms of their structure and interactions at a micro scale. Molecular Dynamics is also referred to as a complement to conventional experiments, making us to discover or understand something new. In MD, the continuous configuration of the system is through the integration of Newton's law of motion. These laws are stated below;

1. A body in motion not influenced by any forces will turn to move in constant velocity.
2. Force equals the rate of change of momentum.

We can therefore obtain the trajectory of our system by solving the Newton's second law (Anderson et al., 2005);

$$F_i = m_i a_i = m_i \frac{d^2 r_i}{dt^2} \tag{2.1}$$

Where F is the force exerted on particle i, m_i is the mass, a is the acceleration, r_i is the position of the particle. In terms of the potential energy U, the force can be expressed as;

$$F_i = -\nabla_i U \tag{2.2}$$

So combining Equations (2.1) and (2.2) yields the derivative of potential energy U to change in position as a function of time.

$$m_i \frac{d^2 r_i}{dt^2} = -\nabla_i U \quad 2.3$$

By stepwise numerical integration using the finite difference method, the trajectories and momenta of the system of particles are produced. Details of this will be given in the energy minimization section of this chapter

2.1.1) Force Fields

For this study, we used one of the best software for Molecular Dynamics simulation (MDS) and Non Equilibrium Molecular Dynamics (NEMD), which is the GRONINGEN Machine for Chemical Simulation (GROMACS) version 5.0.1. After a careful study of the various force-fields, the Transferable Potentials for Phase Equilibria (TRAPPE) Force Field was selected. Force field as used in computational chemistry refers to the functional form (forces due to covalent bonds and long range electrostatics or van der Waals) and parameter (atom types, bonds, angles, dihedrals) in calculating the potential energy of a system of atoms in molecular dynamic simulations.

The TRAPPE is well suited for describing intermolecular interactions as well as accurately predicting relative binding free energies for hydrocarbons (Martin et al., 2008). This force field was developed in the laboratory by the Siepmann Group (2016) over a course of several years and has also been described in detail. The potential energy U of the system is calculated by the summation of both bonded and non-bonded terms, bond bending, bond stretching and torsion (Martin et al., 2008).

$$E(r^N) = E_{\text{bonds}} + E_{\text{angles}} + E_{\text{dihedrals}} + E_{\text{nonbonded}}$$

(2.4)

$$E_{\text{bonds}} = \sum_{\text{bonds}} K_r (r - r_0)^2 \quad (2.5)$$

$$E_{\text{angles}} = \sum_{\text{angles}} k_\theta (\theta - \theta_0)^2 \quad (2.6)$$

$$E(\varphi) = V_1 / 2 [1 + \cos(\varphi + f_1)] + V_2 / 2 [1 - \cos(2\varphi + f_2)] + V_3 / 2 [1 + \cos(3\varphi + f_3)] \quad (2.7)$$

$$E_{\text{nonbonded}} = \sum_{i>j} f_{ij} \left(\frac{A_{ij}}{r_{ij}^{12}} - \frac{C_{ij}}{r_{ij}^6} + \frac{q_i q_j e^2}{4\pi \epsilon_0 r_{ij}} \right) \quad (2.8)$$

With the combining rules $A_{ij} = \sqrt{A_{ii}A_{jj}}$ and $C_{ij} = \sqrt{C_{ii}C_{jj}}$. (2.9)

$$f_{(ij)} = 0.5 \text{ if } i, j \text{ are } 1, 4; \text{ otherwise, } f_{(ij)} = 1.0$$

The above equations show the bonded, non-bonded, angles and dihedrals used in the TRAPPE potential for atomic and molecular interactions. Fig 2.1 shows different types of bond movements as force is applied to the molecules. There are three major types of bonded interactions : bond stretching where molecules moves on parallel direction away from each other,

bond angle bending where there is movements at an angle and dihedrals rotation where long chain molecules turn to rotate along a plane.

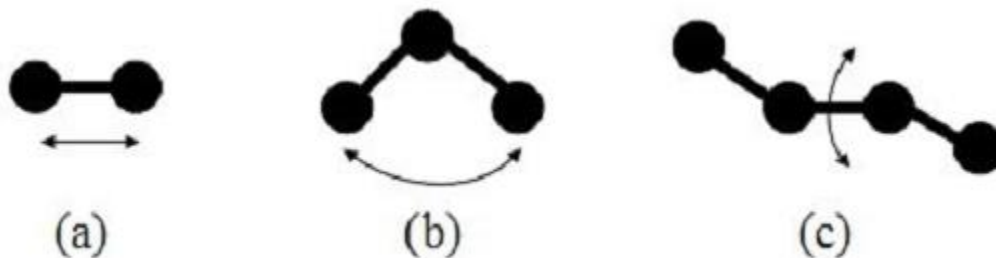


Fig 2.1) Schematic diagram of the various bonded interactions. a) Bond stretching b) bond angle bending and c) dihedral rotation.

2.1.2) Energy Minimization

Having gotten our force fields parameters and coordinate files for the system, the next step is to minimize the total energy of the system to avoid simulation crash.

It is also referred to as geometry optimization. The main goal is to find a minimum potential energy surface from a larger energy initial structure. As shown in the Fig 2.2 below, the energy is reduced in a step by step manner (from steps 2 to 3 to 4) until a local or global minimum on the surfaces potential energy is reached (Frenkel and Smit., 2002; Kadau et al., 2004).

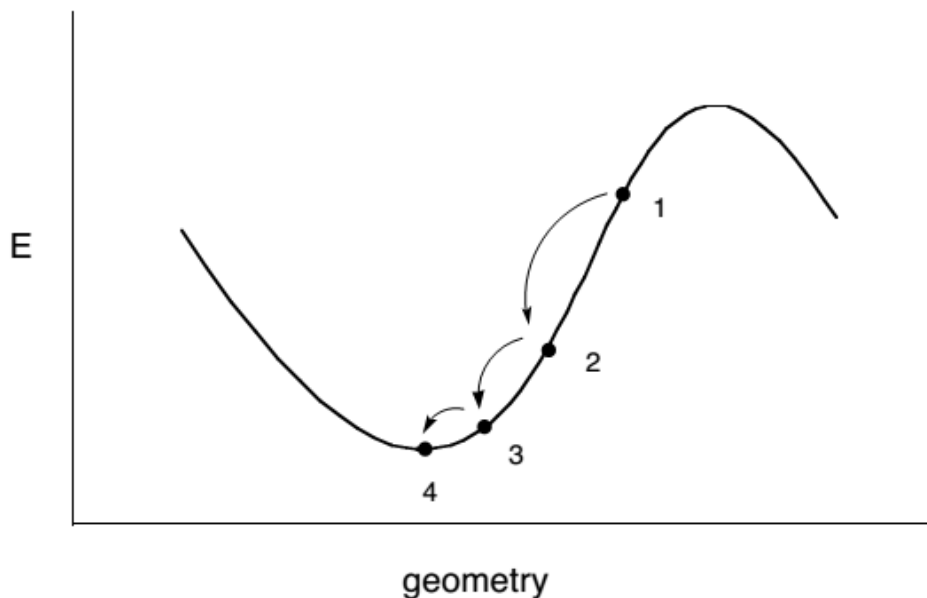


Fig 2.2: Graph illustrating steps in energy minimization from unstable point 1 to a more stable point 4 (Jean et al., 2015).

At the start of the simulation, the molecules and atoms might be wrongly packed, giving room for incorrect bond lengths, or stresses. All these will turn to increase the potential energy, so minimization methods is applied by determining the energy and the slope of the function at point 1. A positive slope is an indication that the coordinate is too large while a negative slope shows that coordinates are too small. Numerical minimization technique then tries to adjust the coordinates. If the slope is not zero a further adjustment is done as shown in Fig 2.2 from 1 to 4 , where 4 is the lowest energy point (local minima) hence minimization is reached .

There are many different algorithms for actually adjusting the geometry to obtain the minimum. Some main algorithms are: Steepest Descent, Newton-Raphson, and Conjugate Gradient. Most used an iterative formula and continue in a step wise order. These are all based on the formula type: $X_{\text{new}} = X_{\text{old}} + \text{correction}$.

The steepest descent algorithm was first used to ensure minimization until a maximum force less than 1,000KJ/mol is reached. This algorithm is not the most efficient but it is easy to implement as well as robust (Gromacs 5.0.1).

In the Steepest Descent, the Forces F and the Potential energy U are first calculated. The algorithm stops when the forces have converged to the user specified number ($<1,000\text{KJ/Mol}$ in our case) or when we have bad contacts or very small minimization steps (Gromacs 5.0.1). L-BFGS Energy minimization method was further used; This method works by successively creating better approximations of the inverse Hessian Matrix, and thus moving the system closer to the current estimated minimum. However it has one disadvantage that it is not practical for very large systems like biomolecules (Gromacs 5.0.1). The minimization was set for 50,000 steps for maximum force to converge below 10KJ/mol.

Another very important parameter was the bonds constraints for both methane molecules and water molecules. Two main bond constraints algorithm has been setup in GROMACS; SHAKE and LINCS algorithms. The SHAKE algorithm changes a set of unconstrained coordinates \mathbf{r}' to a set of coordinates \mathbf{r}'' that fulfills a list of distance constraints, using a set \mathbf{r} reference. (Gromacs 5.0.1)

The LINCS which is also an algorithm on the other hand resets bonds to their correct lengths after an unconstrained update (Hess, B.P-LINCS, 2007). It is a non-iterative method that always uses two steps. This method is more stable and faster than the SHAKE and is suitable for isolated angle constraints such as the proton angle in OH. With such advantages LINCS was used for the Methane-water simulation, with just one iteration step.

2.1.3) Non Bonded Interactions and Long Range Electrostatics

a) Non-bonded Interactions

Since we deal with different atom types, a good algorithm needs to be set to deal with the interaction between two different molecules some distance apart. In GROMACS non-bonded interactions are pair-additive and Centro-symmetric (Gromacs 5.0.1)

$$V(\mathbf{r}_1, \dots, \mathbf{r}_N) = \sum_{i < j} V_{ij}(\mathbf{r}_{ij});$$
$$\mathbf{F}_i = - \sum_j \frac{dV_{ij}(r_{ij})}{dr_{ij}} \frac{\mathbf{r}_{ij}}{r_{ij}} = -\mathbf{F}_j$$

2.10

Where i and j are two atoms apart with i exerting equal but opposite force \mathbf{F} on j , as defined by Newton's third law of motion which states that "For every action, there is an equal and opposite reaction".

The non-bonded interactions contain a dispersion term, a repulsion term and a Coulomb term.

The dispersion and repulsion terms have been combined in the Lennard-Jones interaction which is widely used in Molecular Dynamic simulations, and the Coulomb term in partially charged atoms (Gromacs 5.0.1).

The Lennard-Jones interactions between two atoms can be given by;

$$V_{LJ}(r_{ij}) = \frac{C_{ij}^{(12)}}{r_{ij}^{12}} - \frac{C_{ij}^{(6)}}{r_{ij}^6}$$

2.11

The parameters $C_{ij}(12)$ and $C_{ij}(6)$ depends on pairs of atom types, and they are taken from a matrix of the LJ-parameters (Frenkel and Smit, 2002; Kadau et al., 2004) r is the distance between the atom pairs.

The force therefore derived from this potential is given by;

$$\mathbf{F}_i(\mathbf{r}_{ij}) = \left(12 \frac{C_{ij}^{(12)}}{r_{ij}^{13}} - 6 \frac{C_{ij}^{(6)}}{r_{ij}^7} \right) \frac{\mathbf{r}_{ij}}{r_{ij}} \quad 2.12$$

Furthermore, the coulomb interaction between two charged particles is also considered. Since our atoms have partial charges, there is force acting on each other. The interaction is given by;

$$V_c(r_{ij}) = f \frac{q_i q_j}{\epsilon_r r_{ij}} \quad 2.13$$

$$f = \frac{1}{4\pi\epsilon_0} = 138.935 \text{ 485 (} \quad 2.14$$

With resulting force of

$$\mathbf{F}_i(\mathbf{r}_{ij}) = f \frac{q_i q_j}{\epsilon_r r_{ij}^2} \frac{\mathbf{r}_{ij}}{r_{ij}} \quad 2.15$$

Where q is the charge on both atoms i and j , r is their distance apart.

b) Long Range Electrostatics

Two main methods are being widely used; the Ewald summation named after Paul Peter Ewald and the Particle Mesh Ewald (PME) which is a modified Ewald summation.

The Ewald summation computes long range interactions in periodic systems. The long range calculation is a special case of the Poisson summation formula replacing real space summation of interaction energies with a corresponding summation in Fourier space. The PME uses the Fourier transform because of its rapid convergence of the energy compared to a direct summation and hence accurate and reasonably fast for computing long range interaction.

However, to calculate with accuracy the total coulombic interaction, this method requires charge neutrality of the system. The major difference between the PME and original Ewald summation is the replacement of the direct summation of interaction energy between point particles rather than for short range terms and long range terms.

2.1.4) Equilibration

Ensuring equilibration for our system before simulation is not an easy task especially for small systems whose properties fluctuate considerably. Equilibration is simply arranging of atoms and removing any bad contacts or unwanted forces.

Equilibration is usually done in two phases. The first phase is under an NVT ensemble (constant Number of particles, Volume and Temperature). This is usually known as “Temperature coupling or isothermal-isochoric”. In NVT, the pressure is not considered and so there is no Volume change.

The second phase is under the NPT ensemble (constant Number of Particles, Pressure and Temperature), this is commonly known as “pressure coupling or isobaric-isothermal”. Here the

system is equilibrated at a reference pressure and there is usually a change in the volume of the system due the pressure-volume inverse relationship.

So many temperature and pressure coupling techniques have been developed over the years and use of each will be dependent on the kind of system you intend to study.

2.1.5) Temperature Coupling

There are various reasons why we need to control the temperature of which might be due to a drifting as a consequence of force truncation and motion integration errors, frictional forces or heating due to external sources.

In molecular dynamics we can simulate a constant temperature system using the Berendsen weak-coupling scheme, the extended Nose-Hoover or the velocity-rescaling scheme. The advantages of each can be briefly explained below.

The Berendsen algorithm is usually referred to as a weak coupling because when the system reaches equilibrium the temperature might still fluctuate. It is a weak coupling with first-order kinetics to an external heat bath with given temperature T_0 . This little deviation in the temperature of the system can be corrected by this equation;

$$\frac{dT}{dt} = \frac{T_0 - T}{\tau} \tag{2.16}$$

Where τ is the time constant, this shows that the temperature decays exponentially with τ .

Berendsen thermostat is usually not used for long simulations because it suppresses the fluctuations of the kinetic energy hence not generating a correct canonical ensemble. Hence it is mostly used just to equilibrate the system for few picoseconds before the production run properly. However, the Berendsen Thermostat has the advantage that the strength of the coupling can be varied and adjusted to the user requirements.

The Velocity re-scaling temperature coupling is a modification of the Berendsen thermostat with an added stochastic term that distributes a correct kinetic energy according to;

$$dK = (K_0 - K) \frac{dt}{\tau_T} + 2 \sqrt{\frac{K K_0}{N_f}} \frac{dW}{\sqrt{\tau_T}},$$

2.17

Where N_f is the number of degrees of freedom, dW is the Weiner process, K is the kinetic energy (Zhao et al., 2016).. This thermostat produces a first order decay of temperature, no oscillations and a correct canonical ensemble.

The Anderson Thermostat developed by Anderson couple the system to a heat bath using stochastic collisions that act occasionally on randomly selected particles (Zhao et al., 2016).

In details, the equations of motion of the N particles with Volume V are simply the Hamiltonian equations with $H = \sum \mathbf{p}^2_i / 2m_i + \varphi(\mathbf{q})$

$$\frac{d\mathbf{q}_i}{dt} = \frac{\partial H}{\partial \mathbf{p}_i}, \quad \frac{d\mathbf{p}_i}{dt} = -\frac{\partial H}{\partial \mathbf{q}_i} \quad 2.18$$

With $d\mathbf{p}_i/dt$ being the added stochastic collision term in the equation of motion.

So to carry out the simulation, the Anderson thermostat introduces two main parameters; T and ν , where T is the desired temperature and ν is the frequency of stochastic collisions which is a function of the strength of the coupling to the heat bath. However, if successive collisions are uncorrelated, the distribution of time intervals between two successive stochastic collisions, $P(t; \nu)$, is of Poisson form

$$P(t; \nu) = \nu e^{-\nu t} \quad 2.19$$

Where $P(t; \nu)dt$ is the probability that the next collision will take place in the interval $[t, t + \Delta t]$.

The major disadvantage of the Anderson thermostat is that it destroys momentum transport because of random velocities (hence no continuity of momentum), messes up dynamics and makes it not physical. So using the Anderson thermostat to measure dynamical properties is not a good method.

Since the energy of a system containing N particles fluctuates at a constant temperature. It is important to include an energy fluctuation term in order to simulate such a system. Like in the Anderson thermostat where stochastic collisions are used in simulating the system Temperature, Nose invented an extended Lagrangian formulation containing additional artificial velocities and coordinates. This thermostat is stable and efficient for large scale simulations in which an expensive optimization needs to be carried out a each given time step (Zhao et al., 2016).

The Nose Hoover Thermostat provides a way to simulate a system which is at large times (asymptotically) in the NVT ensemble. The basic principle is to introduce a friction term ζ , which is a fictitious dynamical variable to either accelerate or slow down particles until the required temperature is reached. The friction parameter or the heat bath variable is a fully dynamic quantity with its own momentum (p_ζ) and equation of motion in GROMACS. The equations of motions are:

$$\begin{aligned} m_i \frac{d^2 \mathbf{r}_i}{dt^2} &= \mathbf{f}_i - \zeta m_i \mathbf{v}_i \\ \frac{d\zeta(t)}{dt} &= \frac{1}{Q} \left[\sum_{i=1}^N m_i \frac{\mathbf{v}_i^2}{2} - \frac{3N+1}{2} k_B T \right], \end{aligned} \tag{2.20}$$

Where Q determines the relaxation of the dynamics of the friction, $\zeta(t)$, while T denotes the target temperature. When $d\zeta/dt = 0$, we have a steady state and the kinetic energy is given by $3/2 (N+1)k_B T$ (k_b) as required by equipartition, factor of $3N+1$ instead of $3N$ as there is one more degree of freedom, ζ . We can then note that the temperature is therefore not fixed, rather it *converges to* the target value.

The difference between the weak-coupling scheme and the Nose-Hoover algorithm is that using weak coupling you get a strongly damped *exponential relaxation*, while in the Nose-Hoover there is *oscillatory relaxation (fluctuations)*. Therefore, the actual time to relax the system in Nose-Hoover is several times larger than that of a weak-coupling such as the Berendsen Thermostat. So we can equilibrate our system using a weak coupling method which requires usually shorter time (100ps) and Nose-Hoover method for large time frame as in a production run.

2.1.6) Intergrators

There are two main dynamic integrator schemes in GROMACS which as well have been used by many researchers. They are the Leap Frog integration scheme (Peter et al, 2013) and the Velocity Verlet scheme (Jean et al., 2015).

Both use the finite difference method to solve the Newton laws of motion. The finite difference method is used to generate Molecular Dynamic trajectories with continuous potentials (Jorgensen et al., 1983). The various integrators divide the system into many small steps, each with a time interval.

The various MD integrators divide the system into many small steps, each with a time interval δt . The sum of interaction from all the particles can be used to calculate the total set of interactions on each particle at a given time t . At time t and $t + \delta t$, the force and acceleration are assumed constant, hence they can be determined for new positions. All the afore mentioned algorithms (Verlet, Velocity Verlet and Leap Frog) assume that the positions, velocity and acceleration can be approximated by the Taylor's series

$$\begin{aligned} \mathbf{r}_i(t + \Delta t) &= \mathbf{r}_i(t) + \Delta t \mathbf{v}_i(t) + \frac{\Delta t^2}{2m_i} \mathbf{f}_i(t) + \frac{\Delta t^3}{3!} \ddot{\mathbf{r}}_i(t) + \mathcal{O}(\Delta t^4) \\ \mathbf{v}_i(t + \Delta t) &= \mathbf{v}_i(t) + \frac{\Delta t}{m_i} \mathbf{f}_i(t) + \frac{\Delta t^2}{2} \ddot{\mathbf{v}}_i(t) + \frac{\Delta t^3}{3!} \dddot{\mathbf{v}}_i(t) + \mathcal{O}(\Delta t^4). \end{aligned} \tag{2.21}$$

Where \mathbf{v}_i is the initial velocity ($d\mathbf{S}/dt$, - first derivative of the position), \mathbf{f}_i is the force, \mathbf{f}_i / m_i is the acceleration and m_i is the mass.

The Leap Frog algorithm which was used in our simulation for integrating the equations of motion uses positions \mathbf{r} , at time t and velocities \mathbf{v} at time $t - 1/2\Delta t$; it updates positions and velocities using the forces $\mathbf{F}(t)$ determined by the positions at time t using :

$$\begin{aligned}
\mathbf{v}_i(t + \frac{\Delta t}{2}) &= \mathbf{v}_i(t - \frac{\Delta t}{2}) + \frac{\Delta t}{m_i} \mathbf{f}_i(t) \\
\mathbf{r}_i(t + \Delta t) &= \mathbf{r}_i(t) + \Delta t \mathbf{v}_i(t + \frac{\Delta t}{2}).
\end{aligned}
\tag{2.22}$$

It can be seen that the velocities are updated at half time steps and “leap” ahead the positions.

The current velocities can be given by

$$\mathbf{v}_i(t) = \frac{\mathbf{v}_i(t - \frac{\Delta t}{2}) + \mathbf{v}_i(\Delta t + \frac{\Delta t}{2})}{2}.
\tag{2.23}$$

The Leap Frog produces trajectories that are very similar with the Verlet algorithm and its position-update is given by

$$\mathbf{r}(t + \Delta t) = 2\mathbf{r}(t) - \mathbf{r}(t - \Delta t) + \frac{1}{m} \mathbf{F}(t) \Delta t^2 + O(\Delta t^4)
\tag{2.24}$$

This is of third order differential equation in \mathbf{r} and it is time-reversible (Gromacs 4.6.5). It is also worth noting that the Leap Frog scheme minimizes numerical imprecision and the equations of motion are modified for temperature and pressure coupling.

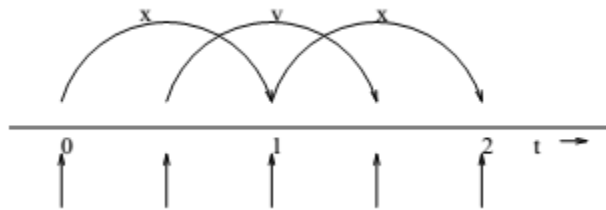


Fig 2.3: Leap Frog integration method.

As shown in Fig 2.3 \mathbf{r} and \mathbf{v} are leaping over each other and that's why this algorithm is termed the “Leap Frog Algorithm”.

2.2) Monte Carlo Simulations

MC simulations have been the first of the classical molecular simulation techniques developed in the early 50's in the seminal work of Metropolis et al. (1953). The development of this technique is strongly correlated to the performances of computers, with a constant increase of scientific publications since the early 90's.

By nature, this method is intimately linked to the statistical mechanics and it is the method of choice to study most of the static properties of molecular systems, as phase equilibria. MC simulations consist of estimating the configuration integral in the configuration space, and determining the associated thermodynamic properties. In a generalized ensemble γ , the generalized partition function Z_γ is given by (Binder, 2014; Landau, 2014):

$$Z_\gamma = \int_{\vec{r}^N} d\vec{r}^N \rho(\vec{r}^N) \quad 2.25$$

Where $\rho(\vec{r}^N)$ is the probability density of the configuration A_i , defined by its positions, \vec{r}^N .

In the γ ensemble, the average of a given observable B is thereby given by :

$$\langle B \rangle = \int d\vec{r}^N \frac{\rho(\vec{r}^N)}{Z_\gamma} B(\vec{r}^N) \quad 2.26$$

Where $\rho(\vec{r}^N) / Z_\gamma$ is the probability of occurrence of a given configuration A_i . The integration cannot be performed analytically in practice. Hence, the Monte Carlo methods of molecular simulation estimate the average quantity $\langle B \rangle$ by performing a numerical integration over N to ∞ configurations of the system. To generate the new configuration from the old one several MC moves are made. These trial moves in MC calculations include; rigid translation move, volume

change and particle insertion/deletion move. For adsorption studies, the Grand Canonical ensemble which uses the particle insertion/deletion moves is widely applied (Martin, 2013).

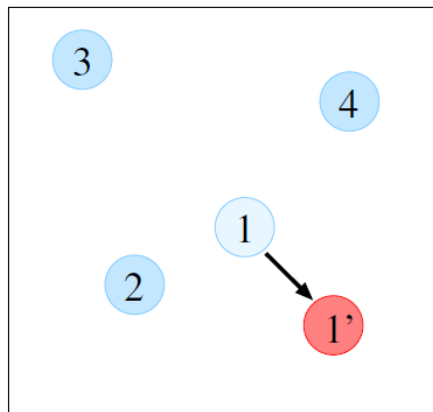


Fig 2.4 Translation move: Random displacement of a particle within the box

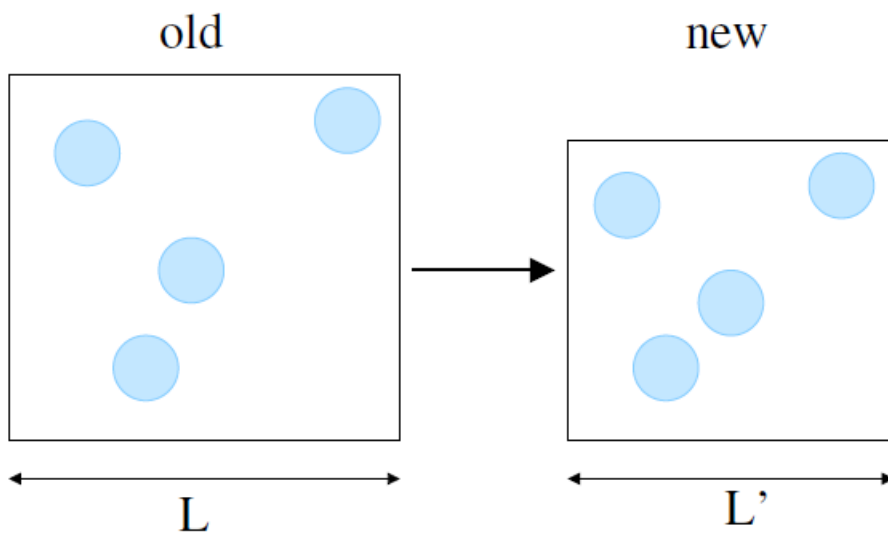


Fig 2.5: Change of volume MC move

CHAPTER THREE

GAS TRANSPORT IN SHALE NANOPORES AND PORE NETWORK MODELLING

3.1 Gas Transport in Kerogen

Kerogen is a solid organic matter with a very complex chemical structure, which is a major constituent in oil shales and other sedimentary rocks. Oil and gas companies as well as academia have devoted tremendous efforts to find ways in exploiting shale gas reservoirs economically, especially at the down turn of oil prices. However, since no two reservoirs are the same as well as its mineralogical and flow properties, new production design is always needed. For shale gas reservoirs which are known of having very high TOC, the type and composition of hydrocarbons and kerogen from which oil is formed turn to differ. The type of kerogen, its chemical composition and properties will change with respect to its depositional environment, whether it is marine, lacustrine or continental (Tissot et al., 1974). The chemical and structural composition of kerogen will change as the maturation process take place. Some very common experimental techniques used for kerogen studies include, Rock-Eval pyrolysis, resistivity measurements, X-ray, Neutron scattering, vitrine reflectance etc. (Alexander et al., 2011).

Although there are many experimental techniques which are now currently used to identify potential large shale fields, little is understood about the molecular and macroscopic interactions which control flow in shale gas reservoirs. Studying these molecular and microscopic interactions in the laboratory possess a major challenge in both time needed and equipment.

Molecular simulation has proven to be very valuable in the oil and gas industry especially after the shale gas revolution in the United States. This is because the pore sizes at nanoscale which renders Darcy fluid flow inapplicable. At this nanoscale, the mean free path λ of the fluid molecules become almost comparable to the characteristic length L of the flow channel. Therefore, macroscale fluid flow like Darcy Equation cannot be used accurately because the continuum theory breaks down when the Knudsen number $K_n = \lambda/L$ is greater than 0.1 (Roy et al., 2003). Fig 3. 1 shows the different flow regions for given Knudsen numbers.

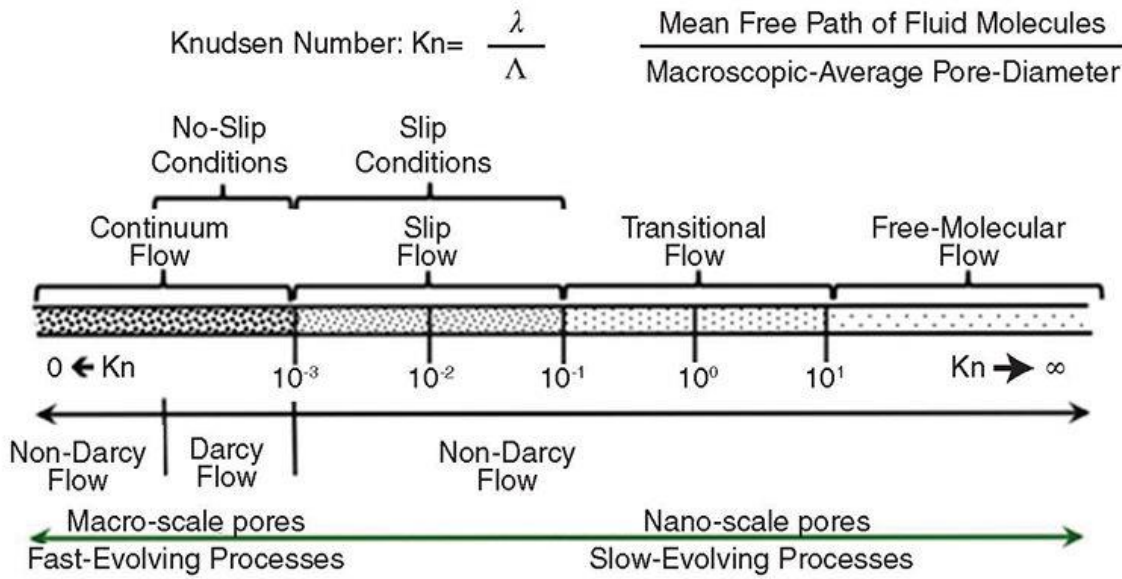


Fig 3.1: Flow regimes (Ivanov et al., 2007)

Also, there are both organic pore (mostly in kerogen) and inorganic pores (from silicates, or limestones). Kerogen presence also constitutes very high amount of the micro porosity in shale gas reservoirs. Figs 3.2 and 3.3 show the presence of organic and inorganic pores for a Bakken shale sample, with finely dispersed kerogen parchments in clay matrix (Javadpour et al., 2007).

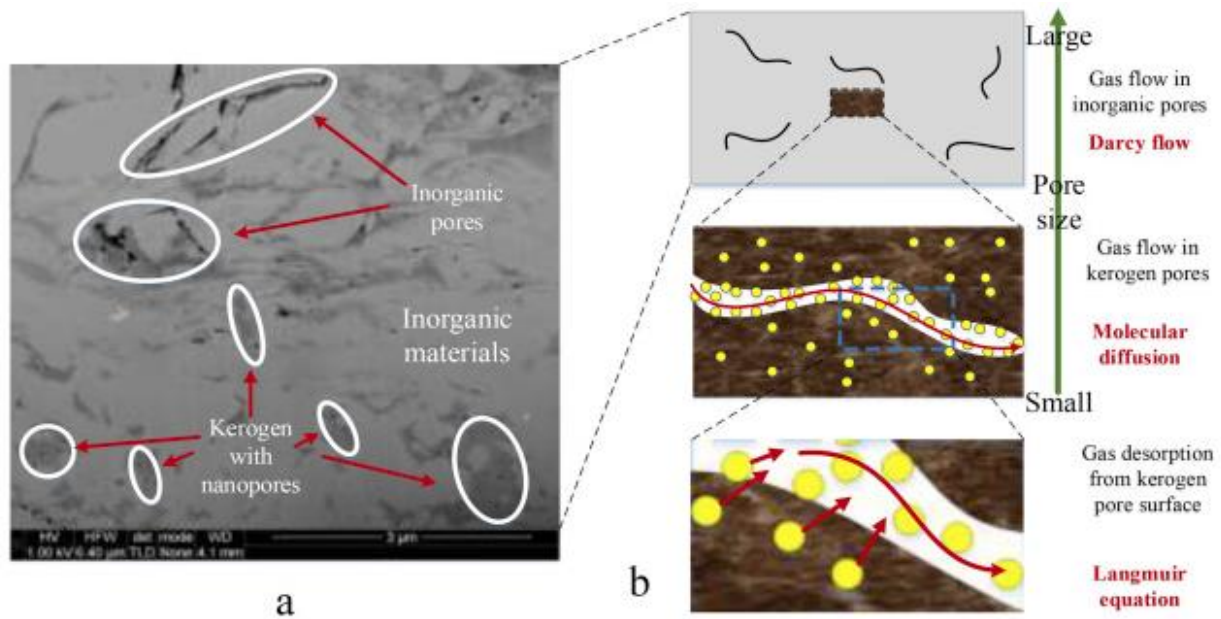


Fig 3.2 (a) 2D FIB/SEM image of shale showing finely dispersed kerogen pockets imbedded in inorganic clays (Ambrose et al., 2012). (b) Schematic of gas desorption and flow pattern in kerogen and inorganic pores (modified from Javadpour et al., 2007; Song, 2010).

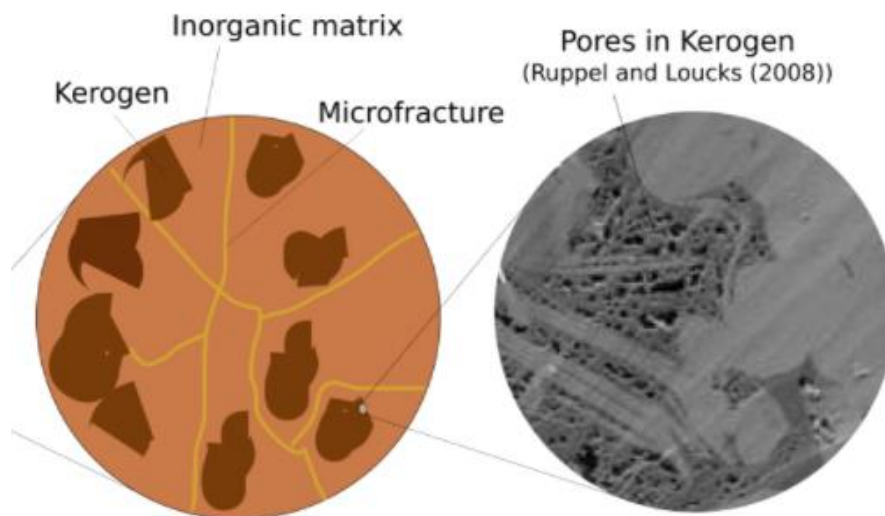


Fig 3.3: Kerogen nanopores (modified from: Ruppel et al., 2008)

It is never possible then to propose a generalized kerogen model due to its high complexity. This complexity makes the modeling of kerogen and other organic solids very challenging. Previous researches have shown that diffusion of gases is slowed down in kerogen matrix as compared to when they flow as bulk fluid. Most of the current studies which focus on fluid flow in organic rich shale have turned to use simplified carbon nanotubes and sheets. Studying fluid transport in simplified carbon-based conduits is not representative of what occurs in the reservoir (Kazemi et al., 2016). The main goal of this work is to determine and quantify the transport properties of methane and ethane in a Type II kerogen matrix using molecular dynamic simulations.

There is a lot of analytical data now in the literature for different kerogen structures and their source rocks. Two dimensional models have been generated and validated with experimental and theoretical results (Behar and Vandenbroucke, 1987; Scouten et al., 1989; Kidena et al., 2008). Some of these validations involve mechanical properties, Raman spectroscopy, and thermal maturity. However, over recent years, 3D structures of kerogen have been generated which makes it even easier to calculate these properties. 2D structures can be converted into 3D structures using molecular dynamic methods and quantum mechanics methods (Ru et al., 2012; Collell et al., 2014). Generation of 3D structure from 2D by quantum mechanics calculations like the Gaussian optimization is solely by determining the most stable conformation (Guan et al., 2015), while multiple molecular dynamic simulations can be used to find the most stable conformations (Ungerer et al., 2014).

Many molecular simulation methods have been used to study transport of fluids in nano-scale, some of which include: boundary-driven non-equilibrium molecular dynamics, equilibrium molecular dynamics and non-equilibrium molecular dynamics. Firoozabadi et al (2015) used

dual control volume grand canonical molecular dynamics (DCV-GCMD) simulations to investigate the transport of methane, carbon dioxide, ethane and butane in varying pore sizes and pressure gradient. They showed that the adsorbed phase is mobile as pressure changes and also the Hagen-Poiseuille equations can significantly underestimate the flow of methane by one order of magnitude. Furthermore, Kazemi et al (2016c) work on methane and argon adsorption affinity showed a decrease in the total mass flux as the average channel pressure increases.

Non equilibrium molecular dynamics (NEMD) simulations are computationally efficient for simulating fluid flow phenomena. Kazemi et al (2016a) used NEMD to investigate adsorption of argon and methane in different nanopore sizes and for different Knudsen numbers. Their results showed that the adsorbed phases contribute to more than 50% of the total mass flux. EMD and BD-NEMD was applied by Collet et al (2015) to study fluid transport with different chemical compositions through kerogen type II model. Their results, computing the Onsagers coefficients for pure and multi-component mixtures, suggested diffusive flow pattern inside the kerogen.

3.2 Microscale Pore Network Modelling

Pore Network Modeling (PNM) has gained wide application over recent years due to the availability of state of the art technology for producing high resolution CT-scanning images. These images can be stacked together to build digital rock which is representative of the original rock. A pore network can then be extracted from the digital rock using many different algorithms available. Pore-scale simulations have greatly improved the understanding of large scale reservoir processes (Xiong et al., 2016). They can produce a cost-effective and accurate prediction of local core scale transport, and at the same allow the flexibility of modeling different scenarios by changing different system parameters such as the pore geometries, fluid properties, and even boundary conditions (Meakin et al., 2009). For the pore space model construction, the

geometry and topology are needed (Xiong et al., 2016), one way of creating this is by imaging techniques such as producing 3D images by stacking the images together. In this method proper segmentation is needed to fully capture all the pore spaces by color contrast. The second method is by assigning certain amount of pores and spacing, and statistically correlating it to give realistic pore model for a given sample.

In this work, NEMD simulations were used to simulate flow of methane and ethane in type II kerogen model. Once the initial configuration was built, energy minimization, constant-temperature constant-volume (NVT) and then constant-temperature constant-pressure (NPT) simulations are performed to obtain the final structure. Transport and self-diffusivities were then calculated. We also created a pore network model for a microscale pore network scenario for a sandstone rock sample, followed by MICP calculations to obtain the capillary pressure and saturation curves. This microscale pore network simulation for an ideal sandstone case is to compare with results from digital rock analysis and to set up a methodology for pore network modelling for ultra-tight formations.

3.3. Model and Methods

3.3.1 Kerogen Molecular Model

In this study, eighteen type II kerogen molecules were used to build a solid state structure. To build a representative model these molecules were placed in a periodic cubic cell with dimensions of 8nm on every side. The Trappe force field was used to describe the long and short range interactions. Once the initial configuration was energy minimized, constant-temperature constant volume (NVT) ensemble simulations were performed at 500K for 4ns. Different conformations were sampled and for each conformation, constant-temperature constant-pressure (NPT) simulations were carried out. The conformation with density of 1.37

gr/cm^3 was selected for our final simulations. This optimum conformation after energy minimization is shown in Fig 3.5. The Velocity Velvet thermostat was used for temperature coupling, Parrinello-Rahman barostat was used for pressure coupling. All simulations were performed for 4ns each with 1 femtosecond time steps. The final density of $1.39 gr/cm^3$ was obtained which is the range of kerogen density reported in literature. Fig 3.4 shows the molecular structure of type II kerogen developed by Urgerer et al (2014).

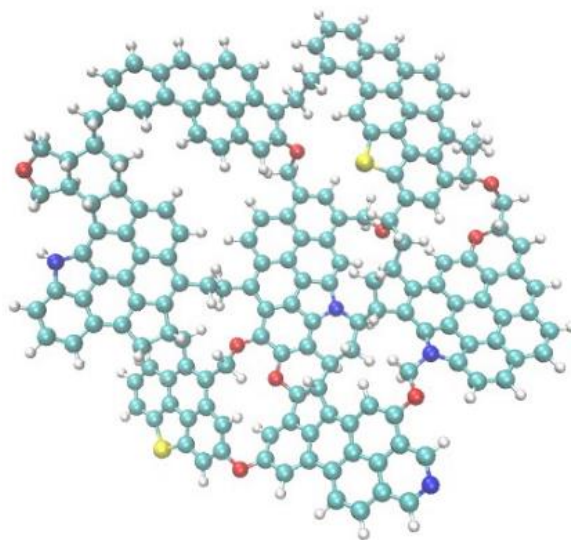


Fig 3.4—Molecular structure of type II kerogen. Cyan color represents carbon, red is oxygen, white hydrogen, blue nitrogen and yellow sulfur atoms.

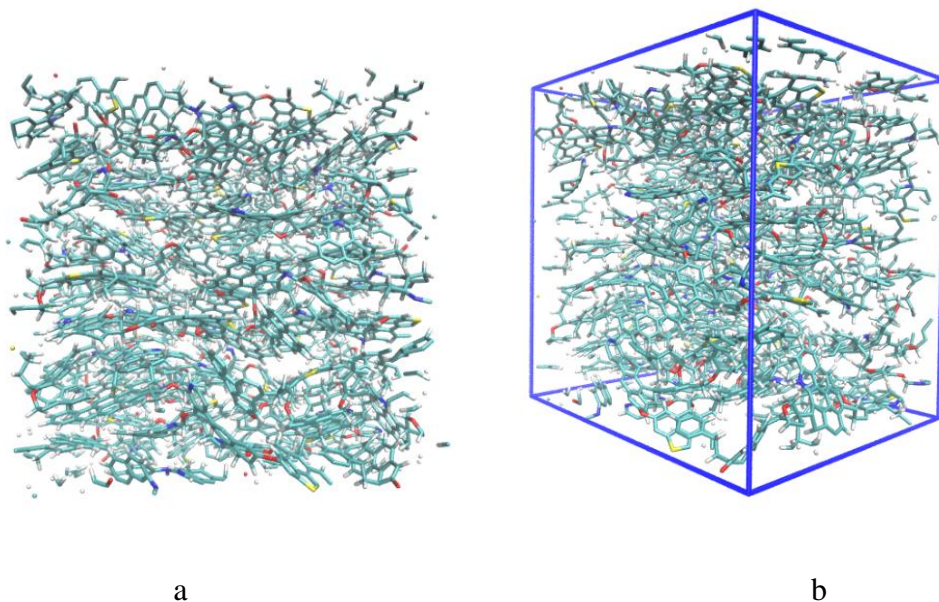


Fig 3.5—final structure of the eighteen kerogen units placed in a simulation box to form nanopores matrix

(a) 2D and (b) 3D representations.

3.3.2 Porosity Characterization

For determining the porosity of the kerogen structure, free volume calculations were carried out. In this method, a probe is used to identify the available pore spaces. A probe size equal to the diameter of a methane molecule was used to determine the available pore volume for gas. The free volume was calculated as 1.5 nm^3 , with a total (bulk) volume of 54.75 nm^3 . This gave a kerogen porosity of 2%.

3.3.3 Diffusion Coefficient

Many studies on diffusion of gases in nanopores have already been reported (Sholl, 2006; Dubbeldam and Snurr, 2007; Smit and Maesen, 2008; Kazeemi et al 2017). Equilibrium Molecular Dynamic simulations are usually carried out to determine the self-diffusivity

coefficients. Self-diffusion, D_s , is defined as the mean square displacement of molecules over time and is defined as (Markus, 2011),

$$D_s = \frac{1}{6N} \lim_{t \rightarrow \infty} \frac{d}{dt} \left\langle \sum_{i=1}^n [\vec{r}_i(t) - \vec{r}_i(0)]^2 \right\rangle, \quad (3.1)$$

This diffusivity equation is the Einstein diffusivity. where N is the number molecules and $\vec{r}_i(t)$ is the displacement vector for the i -th molecule at time t . The six (6) shows that it is in 3 dimensions and the angular bracket represents the ensemble average quantity.

We can equally calculate the transport coefficients from the molecular flux in NEMD simulations by using the following equation;

$$D_t = \frac{k_B T j}{\hat{\rho} F}, \quad (3.2)$$

where k_B is the Boltzmann constant, $\hat{\rho}$ is the average gas density, and F is the applied external force.

For the molecular dynamics simulations, methane and ethane are treated as Leonard-Jones fluid and modeled with the LJ-12-6 potential. A cut off distance of 14 Angstroms is used for all the production runs.

NEMD simulations are performed at 4,000psi and 300K which represents the pore pressure control condition. At this condition five external forces of 0.02, 0.04, 0.1, 0.15 and 0.2 $\frac{kcal}{mol.ang}$ are applied to the inlet region. Simulations are performed for 5 ns with a timestep of 1 fs. The exerted force to the molecules is proportional to pressure drop as described by (Zhu et al., 2002)

$$\Delta P \propto \frac{NF}{A}, \quad (3.3)$$

Where A is the area perpendicular to the applied force. Determining the actual pressure gradient in NEMD simulations is not straightforward. Therefore, to compare the molecular fluxes and velocities in different pressure gradients, the term NF/AL , which is proportional to pressure gradient, is used. The number of molecules at the inlet region is calculated at each time step and averaged over the total simulation time.

3.4. Pore Network Model Construction

For the construction of the model, OpenPNM Delaunay network (Loera et al., 2010; Berg et al., 2008) and voronoi geometry objects were employed. Five hundred randomly distributed pores are placed in a domain size of $10 \mu\text{m} \times 10 \mu\text{m} \times 10 \mu\text{m}$. As explained by Gostick et al (2013), the pores are distributed randomly but with increased density to counteract the higher porosities introduced by the voronoi method. Pore throats are then created by connecting nearest neighbor pores according to a Delaunay triangulation and then storing the connections in an adjacency matrix. Figs. 3.6 and 3.7 show the pore network with all the connecting throats and from the figures there is high distribution of pores around the center of the model.

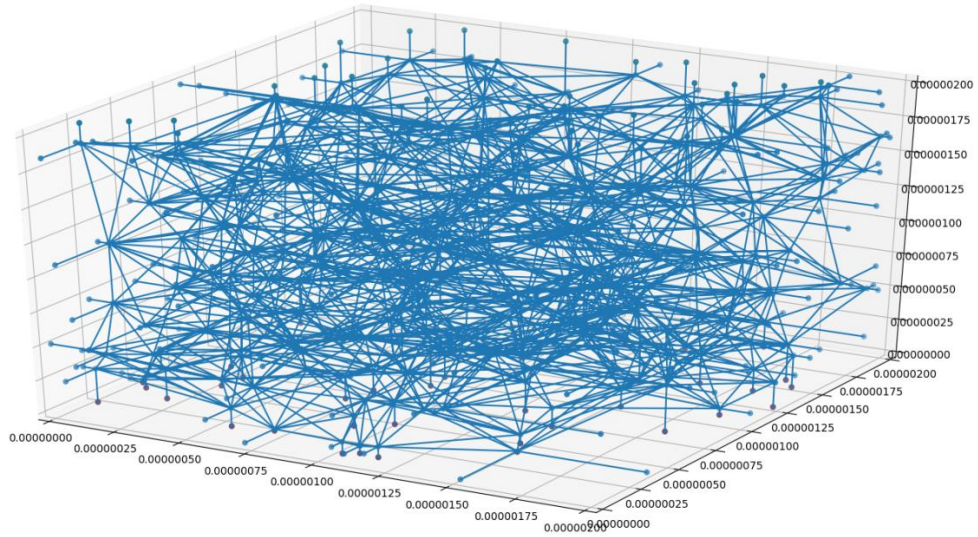


Fig 3.6: Pore network model created using the Delaunay triangulation.

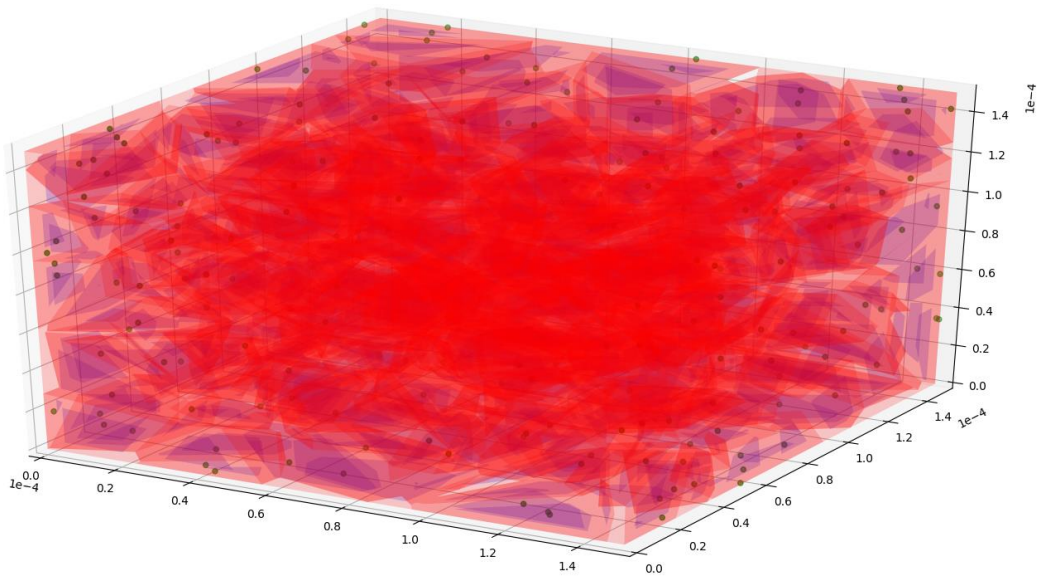


Fig 3.7: Pore network model showing the distribution of the pore spaces in a sandstone model

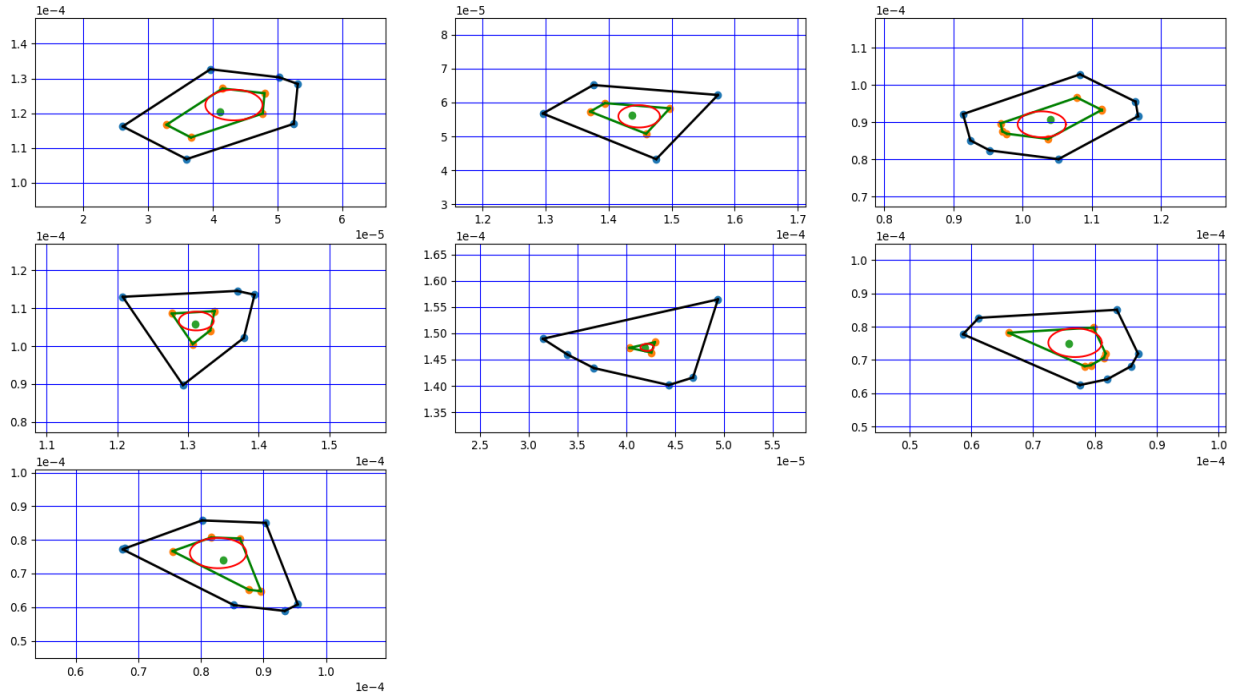
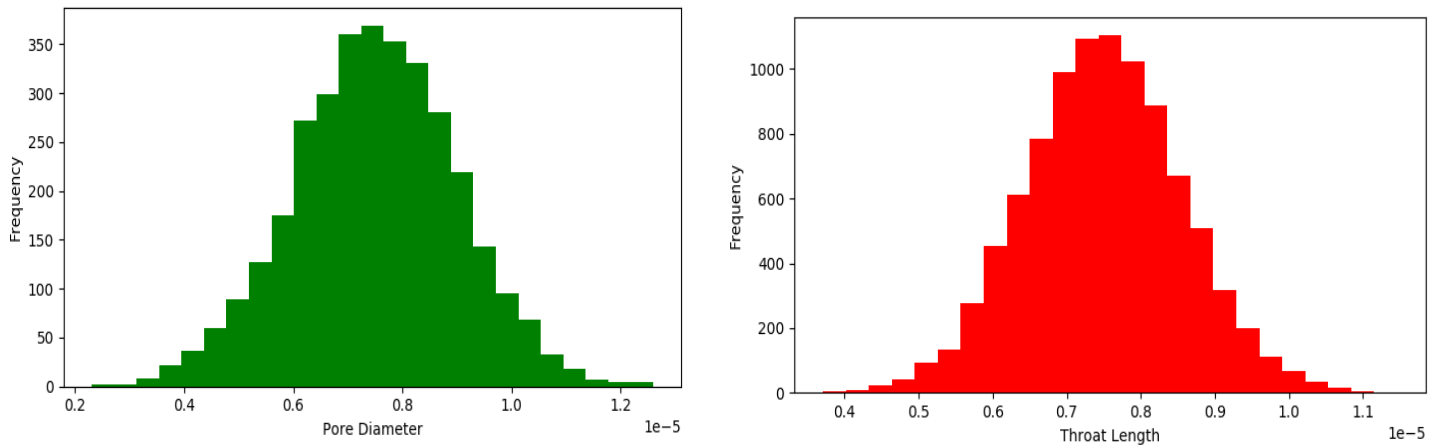


Fig 3.8: Pore connectivity by the Delaunay triangulation method.

The blue points in Fig 3.8 show the center pore connecting to neighboring pores in different ways based on the number of pores surrounding and their relative distances. Fig 3.9 shows a histogram of the pore diameter and throat length and throat diameter. From the figure, most of the pores have diameters of 8 micrometers and the throat diameter of about 3 to 4 micrometers.



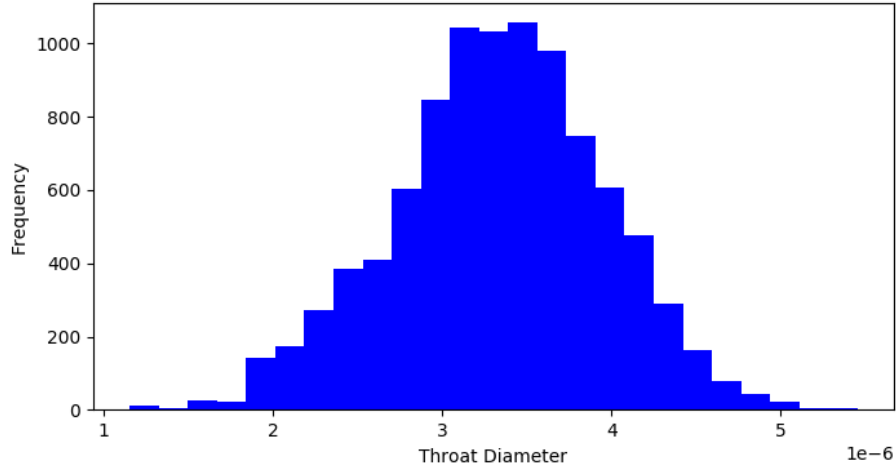


Fig 3.9: Pore and throat size distribution for created model.

Building the pore network model porosity calculation was carried out in all directions and also Mercury Injection Capillary Pressure (MICP) simulations were implemented. The percolation algorithm used represents drainage of a wetting phase by invasion of a non-wetting phase. The non-wetting phase in this case is mercury and the wetting phase air. This process is typically simulated by starting to invade the accessible throats of the dry network belonging to the paths of least resistance. The resistance to flow is based on the capillary entry pressure which is determined by the Washburn equation. The simulation continues until the entire network is filled. The Washburn Equation is given as;

$$P_{c=} - 2\sigma \cdot \frac{\cos\theta}{r} \quad (3.4)$$

3.5 Results And Discussions

3.5.1 Methane and Ethane Transport Diffusivity

Methane and ethane diffuses along the connected pore spaces due to pressure gradient. Fig 3.10 shows methane and ethane transport after 2ns simulation time at temperature of 350K, pressure

of 4,000psi, under an external force factor of 0.02. From Fig 3.10 (a&b), we see that methane has a higher diffusivity than ethane. Most of the ethane molecules are trapped in the kerogen nanopores due to its higher affinity for adsorption than methane. Hence methane is capable of flowing across the nanopores with less resistance. The purple balls represent methane molecules as shown in Fig 3.10a, while the double purples connected with a bond represent two carbon atoms for the ethane molecules as seen in Fig 3.10b.

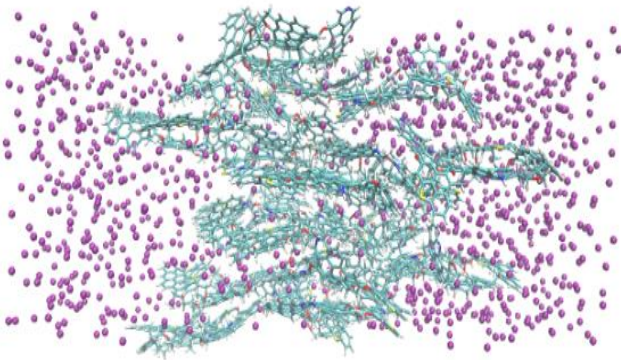


Fig 3.10a) Methane flow in kerogen after 2ns

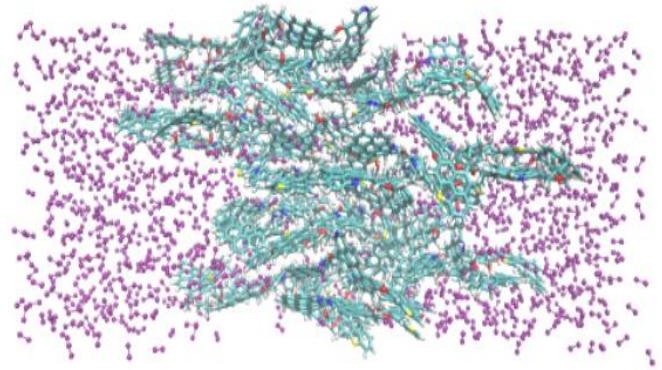


Fig 3.10b) Ethane flow in kerogen after 2ns

Transport diffusion coefficients which are shown in Figs. 3.11 and 3.12 below are computed for a pressure differential factor of 0.02 to 0.2. As the pressure gradient increases, the transport diffusion coefficients increase from 0.03×10^{-7} to $1.81 \times 10^{-7} \text{ m}^2/\text{s}$ for methane (Fig 3.11), and from 0.006×10^{-7} to $0.61 \times 10^{-7} \text{ m}^2/\text{s}$ for ethane (Fig 3.12).

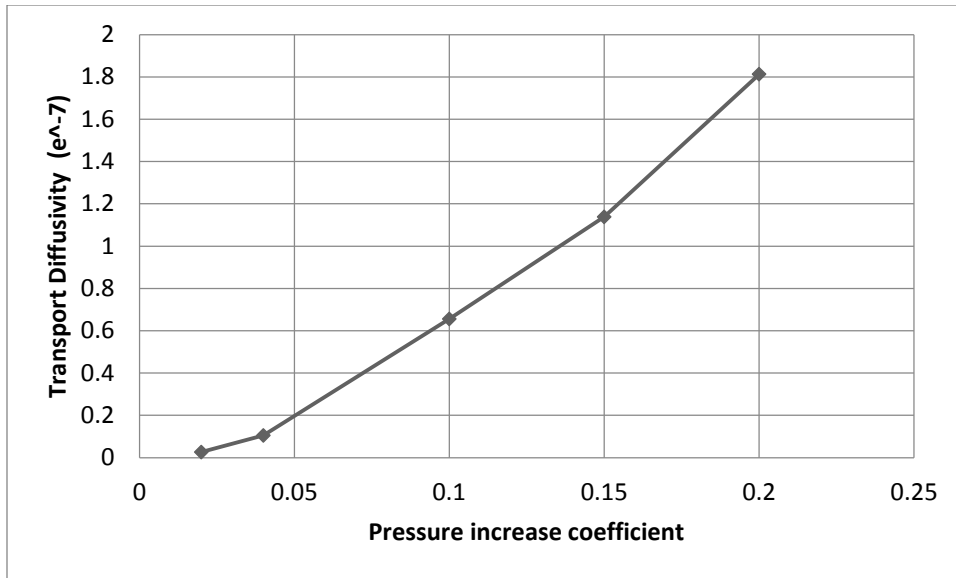


Fig 3.11: Methane diffusion coefficients vs. pressure.

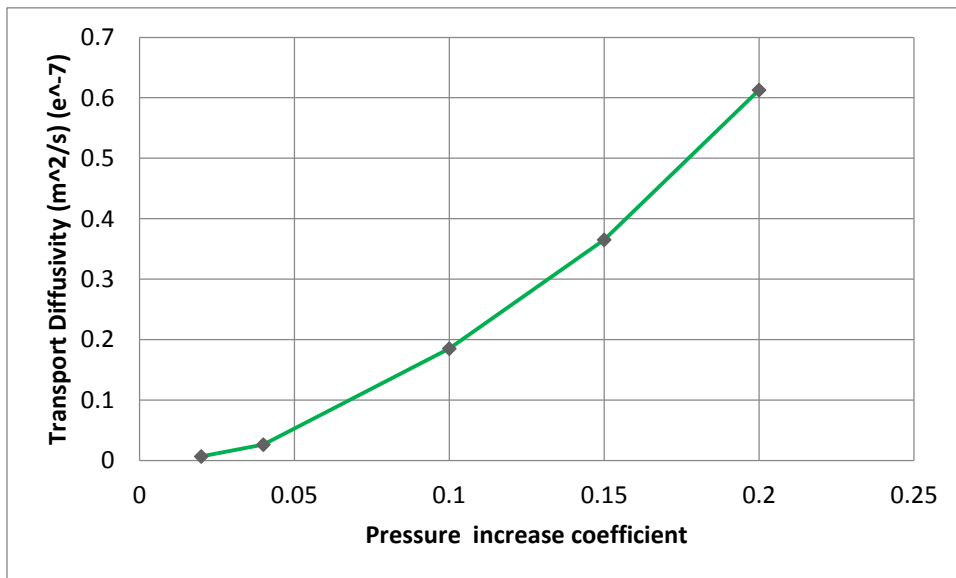


Fig 3.12: Ethane diffusion coefficients vs. pressure.

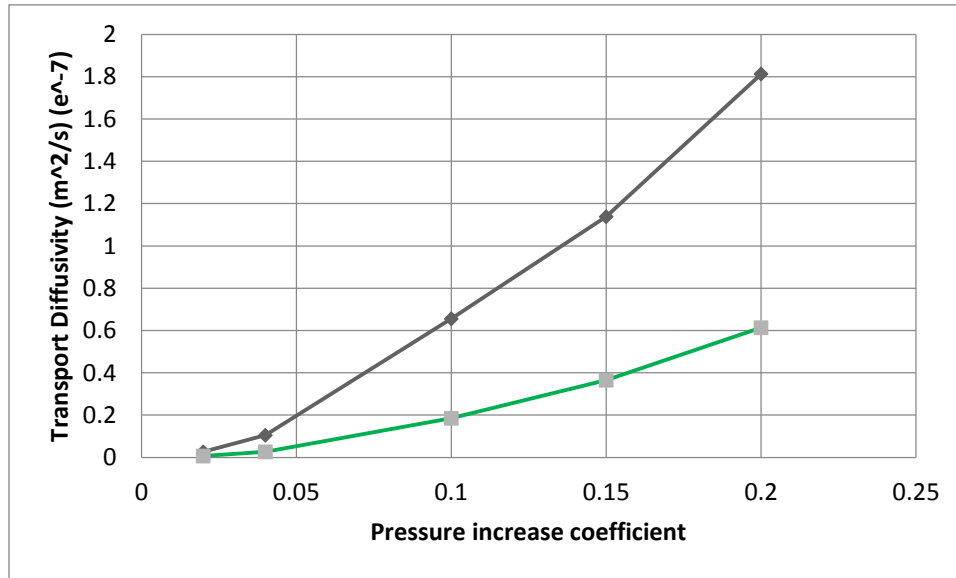


Fig 3.13: Methane and Ethane diffusion coefficients vs. pressure.

3.5.2. Porosity and MICP

The results of the MICP simulation can be seen from Fig 3.15. A smooth trend can be observed which signifies that most of the pore has uniform sizes. The capillary entry pressure starts around 150,000 Pa (21.75 psi). The average porosity from Fig 3.14 is around 0.14 in the xyz directions. These simulations were carried out using the pore network modeling code which is source free for pore network modeling.

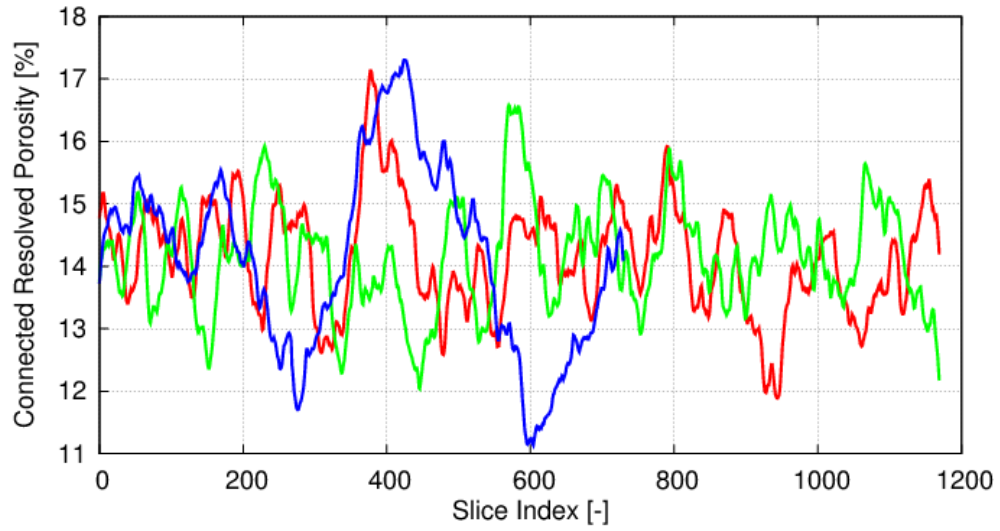


Fig 3.14: Porosity calculation in xyz directions for a sandstone model (blue (z-axis), red (y-axis) and green (x-axis)

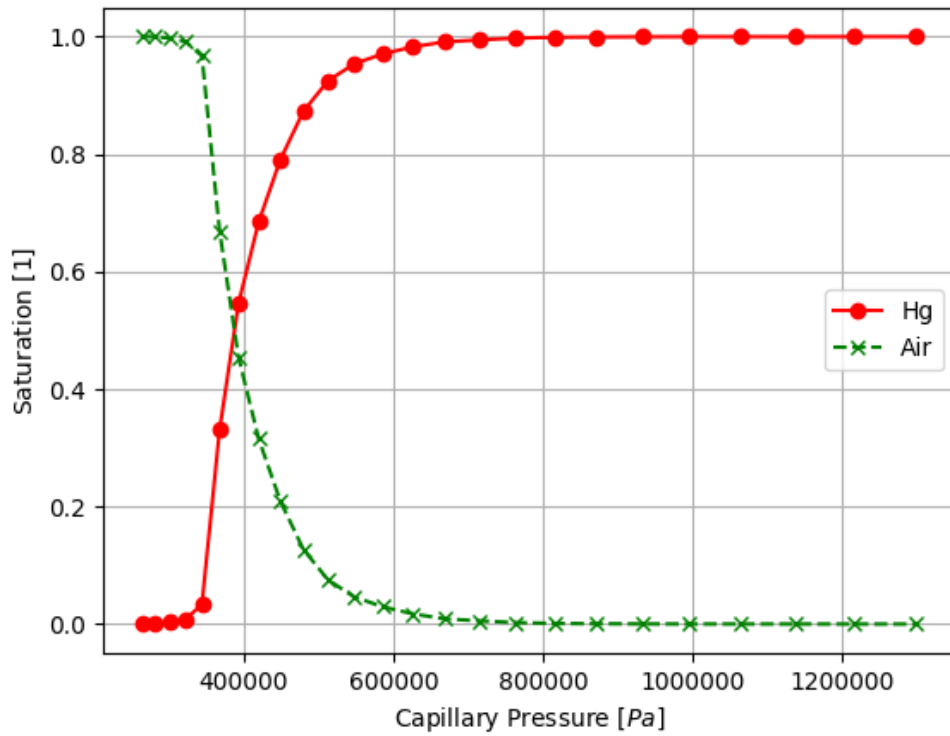


Fig 3.15: Capillary pressure curve vs saturation for invading and defending phases.

3.6. Conclusions

In this study, transport diffusivities of methane and ethane in a three dimensional type II kerogen model are studied using non equilibrium molecular dynamics simulations. The kerogen model prepared by Urgerer et al. (2014) is used in this study. From the studies the following conclusions have been made;

- 1) Methane has a higher diffusivity in kerogen than ethane which is due to its smaller molecular weight.
- 2) Molecular Simulations can be used to study gas behavior in nanoscale environment which is a huge challenge experimentally.
- 3) Pore network modeling serves a component in studying rock and fluid properties at a mesoscale.

CHAPTER FOUR

MOLECULAR SIMULATION OF METHANE, ETHANE AND CO₂ ADSORPTION IN SHALE GAS SYSTEMS

Shale gas reservoirs which have shown enormous potential over recent years are very complex systems that contain heterogeneous organic 3D pore networks with great amount of surface area contained in the micropores. Inside these tiny pores, there exist strong interactions between the fluids and the pore surfaces, because the pore space is restricted leading to variation in the molecular distribution (Jin et al., 2016). Shale consists of nanopores which are randomly distributed in both inorganic (silica) and organic matter (kerogen). According to the International Union of Pure and Applied Chemistry (IUPAC), a micropore is a pore having a width of less than 2nm, while on the other hand, a mesopore has a width ranging from 2 to 50nm (Sing et al., 1985). It has been studied that the amount of free fluid is controlled by the porosity and the amount of adsorbed fluid is determined by the material surface. Fig 4.1 shows different scales of the reservoir rock and gas distributions along the pores. For very tight formations, there exist fracture pores which are larger and pore spaces found in the matrix which are usually at the nanoscopic level. Along the fractures, gas is free to move due to larger fracture pore sizes creating easy flow path for lighter hydrocarbons. In the matrix, however, gas is trapped as either dissolved gas in kerogen or adsorption gas on the nanopore walls. This disparity in the distribution of gas is mainly due to the relatively small (nanoscopic) pore sizes in the matrix as compared to the fractures

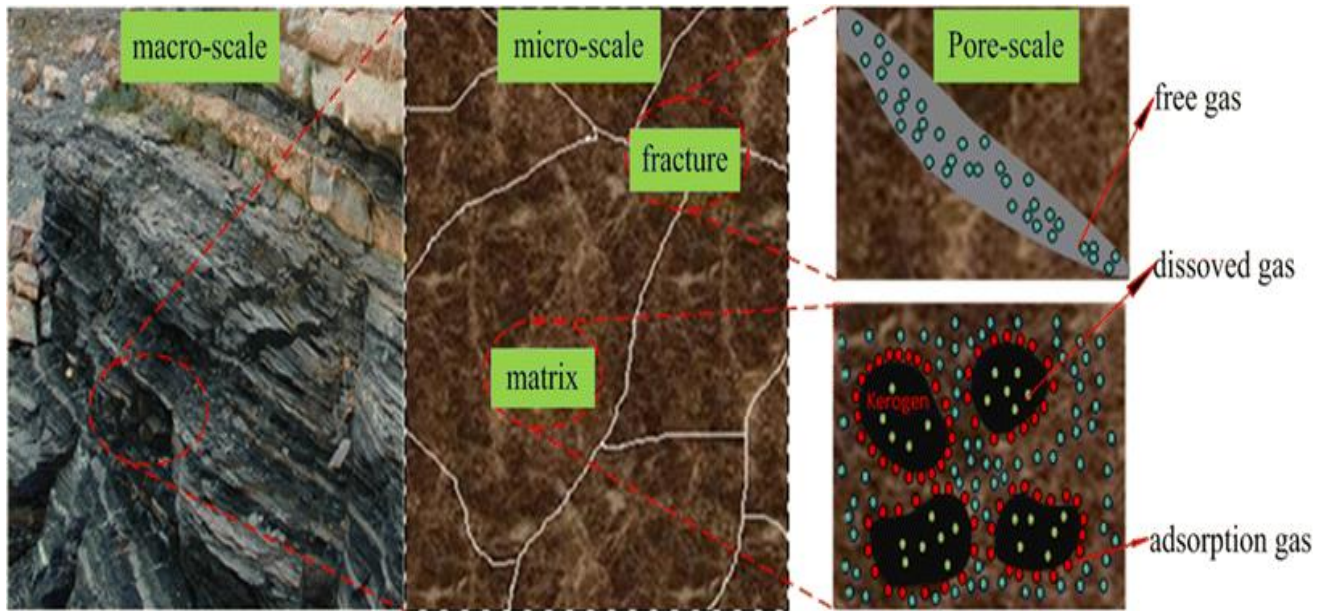


Fig 4.1: Gas distributions in shale formation macro-scale to micro-scale. Free gas is found within fractures and adsorption gas is present in the matrix (Guo et al., 2015).

Zhang et al (2015) in his work proved that stronger adsorption capacity is recorded in better the organic matter type showing that the difference in maturity has no obvious effect on gas adsorption capacity. Furthermore, Ross et al (2013) unveiled that shale with high TOC content leads to higher methane adsorption capacity. Fig 4.2 and 4.3 show even the organic matter has some porosity which might host hydrocarbons (Ambrose et al., 2010; Sondergeld et al., 2010). So for shale plays, it is worth studying the degree of gas adsorption within those shale nanopores.

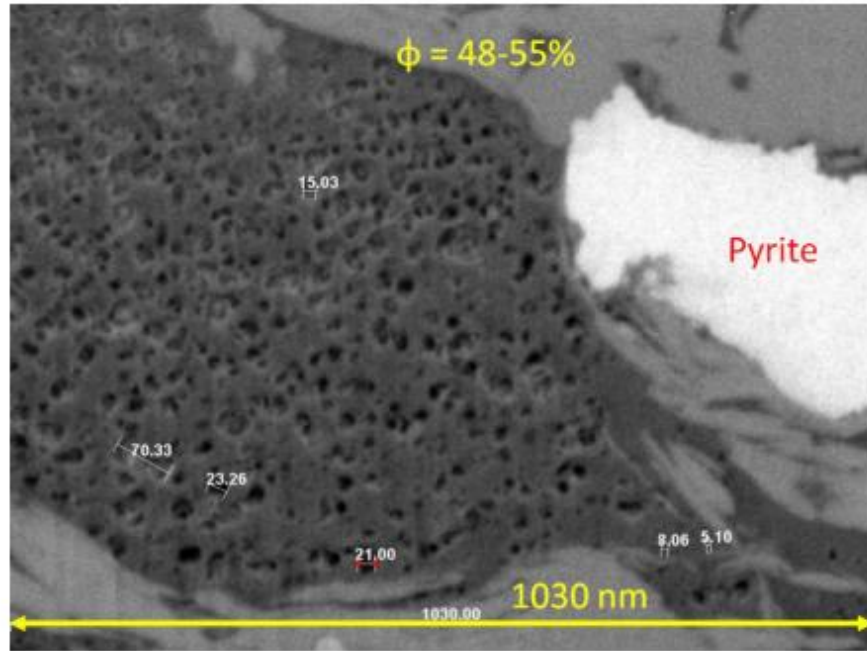


Fig 4.2: SEM image of a kerogen body showing porosity (Sondergeld et al., 2010).

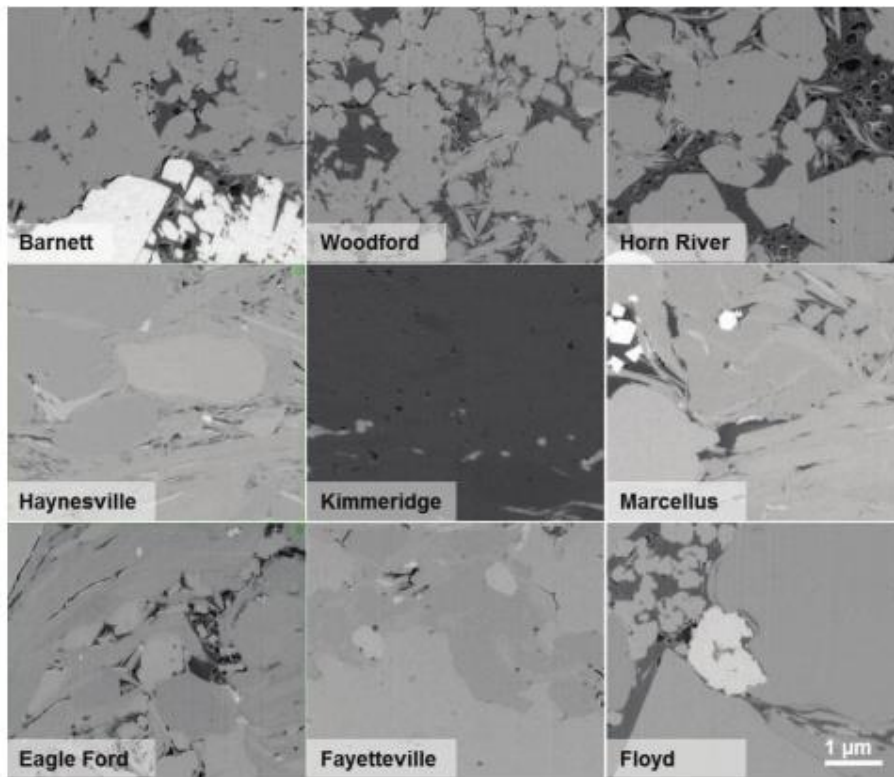


Fig 4.3: BSE image from nine different shale plays (Ambrose et al., 2010)

Adsorption of gases in kerogen and coal have been studied for decades (Bae and Bhatia, 2006, Day et al 2008; Li et al. 2010). Other researchers have developed and improved theoretical models to study gas adsorption phenomena on coal (Lu et al. 2008; Vandamme et al. 2010; Connell et al, 2009, 2012). Different approaches have shown how adsorption rate, adsorption capacity, diffusion and permeability are all related.

Determination of the percentage pore volume in micro and meso scale pores will be largely dependent on the probe gas used. For molecular simulations dealing with porous media, N₂ and Ar are generally used as probes to calculate porosity because they are non-adsorbing gases. CO₂ for example, has tendency to adsorb and maybe affect the uptake of gas in the pores which may lead to overestimation of the pore volume. The variation in pore sizes may also affect the degree of adsorption; in micropores, physisorption at the pore-filling stage will occur, while in larger pores (meso and micro), there exist two stages of adsorption. The first stage is single and multilayer adsorption and the second will be capillary condensation (Wilcox et al., 2012).

In micropores, adsorption is controlled by fluid-wall and fluid-fluid interactions, and hence leading to only a single layer and spatial distribution of molecules. Studies have shown that the density of the adsorbed phase is by far higher than the density of the bulk liquid. There is continuous pore filling in micropores because of the overlapping forces of the pore walls. On the contrary, there is pore condensation which is representative of the gas-liquid transition in mesopores.

Another great challenge in studying adsorption behavior is differentiating between the number of gas molecules that would fill a given volume in the absence of pore walls (absolute) versus the number of molecules that would fill that same volume, but with the introduction of pore-wall

effects at the same temperature and pressure conditions. This is due to the fact that the gas present in nanopores will experience interactions with the pore walls which will in turn influence adsorption properties such as density and packing. There are several terms that are used in the literature to characterize adsorption, i.e., *total gas content*, *absolute*, and *excess* adsorption.

Total gas content is defined as the entire quantity of gas that resides in the pore space at a given temperature and pressure and includes both the gas in the center of the pore (i.e., ‘free’ gas) as well as the gas adsorbed directly to the pore surface. Defining the boundary at which the gas is ‘free’ in the pore versus adsorbed to the surface is difficult, but more easily done with molecular simulation than with experiments. Given a large enough pore with minimal influence of the pore walls, the free gas in the pore center may be thought of as the gas that occupies the same volume of space at a given temperature and pressure as it would in its bulk phase. Theoretically, the free gas is not influenced by the pore walls, or any differently by its neighboring gas molecules as it would be in its bulk phase.

Absolute adsorption is defined as the quantity of gas present only in an adsorbed state. This metric is challenging because of the difficulty in identifying the molecules that are in fact adsorbed and not ‘free’ in the pore space. In practice, this information must include the density of the adsorbed layer, single or multi-layer characteristics, and the overall surface area associated with a given pore volume. This term is often calculated based upon the assumption that the density in the adsorbed layer is equal to the liquid-phase density, which is often an incorrect assumption, especially with adsorbing gases at high pressures and in small pores.

Excess adsorption is defined as the additional amount of gas adsorbed per unit pore volume compared with the amount of gas in the same volume of a given pore in the absence of pore

walls. Gas in the adsorbed phase is higher in density than the same gas in the bulk phase, so subtraction of the expected density of gas in the bulk from the total adsorption yields the additional density of gas in the system as a result of adsorption.

It is important to first understand how to calculate the volume a gas occupies at a given temperature and pressure in the absence of pore walls, which is termed the *bulk* phase. In adsorption studies using Monte Carlo simulations, densities are calculated as a function of fugacity instead of pressure, with fugacity loosely defined as the deviation in the vapor pressure exerted by a real gas from the corresponding ideal gas. In most Monte Carlo software packages, the fugacity (i.e., ‘corrected’ pressure) is calculated using the Peng–Robinson equation of state, with this pressure used in plotting the adsorption isotherms. The Peng-Robinson equation of state is described as;

$$p = \frac{RT}{V_m - b} - \frac{a\alpha}{V_m^2 + 2bV_m - b^2} \quad (3.1)$$

$$a = \frac{0.457235R^2T_c^2}{P_c} \quad (3.2)$$

$$b = \frac{0.457235RT_c}{P_c} \quad (3.3)$$

$$\alpha = (1 + k(1 - T_r^{0.5}))^2 \quad (3.4)$$

$$k = 0.37464 + 1.54226\omega - 0.26992\omega^2 \quad (3.5)$$

$$T_r = \frac{T}{T_c} \quad (3.6)$$

Such that T_c , p_c , and ω are the critical temperature, critical pressure and acentric factor, respectively.

The first step needed in building a kerogen model is the selection of the total number of carbon atoms and also the number of aromatic carbons so as to compare with the aromaticity obtained from XPS and NMR. This determines the H, O, N and S content which is needed to match the elemental analysis and how the functional groups are distributed in the kerogen structure. Step two entails building an initial structure using an appropriate force field which correctly gives the equilibrium bond lengths, angles and dihedrals and also by selecting the level of cross-linking between the different aromatic units.

The initial structure is then subjected to energy minimization to reduce the potential energy given by the force field. The minimized structure is then refined by either changing the positions of the functional groups or the shape of the polyaromatic units. Using molecular dynamics, the structure is then subjected to heating or placed in a temperature bath and then gradual cooling and compression to obtain its true density as reported in experiments.

Grand Canonical Monte Carlo (GCMC) and Non Equilibrium Molecular Dynamics (NEMD) have been used extensively to study diffusion, adsorption and transport of methane in kerogen at reservoir conditions.

GCMC provides the total gas content which is the total amount of gas residing in the pore space at any given pressure – temperature condition. In attempt to examine the effect of pressure, temperature and pore size on methane adsorption in type II Kerogen, Mosher et al (2013), studied methane adsorption in idealized nano-carbon slits with width ranging from 0.4 to 9nm at different pressures and temperature conditions. From their results, they found that the amount of excess adsorption increases with corresponding increase in pressure until a certain pressure, of which it starts decreasing to zero. The decrease in excess adsorption is linked to the fact that no noticeable change in density is observed at higher pressures. The increase and later on decrease

in excess sorption suggests that there exists a maximum adsorption quantity. Increase in temperature yield lesser adsorption as compared to pressures but the total number of adsorbed molecules stayed constant. Varying the slit widths, it was observed by Mosher et al (2016), that larger pores exhibit a lower excess sorption density than smaller pores.

4.1 Simulation Details

Molecular simulation enables us to fully describe the interactions between the gases and the shale matrix without predefining your adsorption pattern. Its main strength is being able to predict and reveal the mechanism of gas adsorption in the microscopic scale.

In this study, we simulated gas adsorption in type II Kerogen matrix, in a 4nm silicate and nano-carbon channel. The system studied consists of CH₄, C₂H₆ and CO₂. Generating realistic model for kerogen is essential for organic shale simulations applied to researches in ultra-tight formations. The initial configuration of the Kerogen model consists of 18 randomly placed Kerogen molecules in a 10 x10x10 nm³ periodic box. The simulation box is shown in Fig 4.4. As the system reaches around equilibrium, the system box reduces to 9.54 9.67 9.72 nm³. Our system is then connected to an imaginary gas reservoir to allow the exchange of gas molecules between the Kerogen matrix and the reservoir. Both Grand Canonical Monte Carlo (GCMC) and Non Equilibrium Molecular Dynamics simulation techniques where applied to calculate the adsorption isotherms and diffusivity for methane, ethane and carbon dioxide respectively. The number of molecules in the kerogen matrix varies depending on the pressure or chemical potential applied.

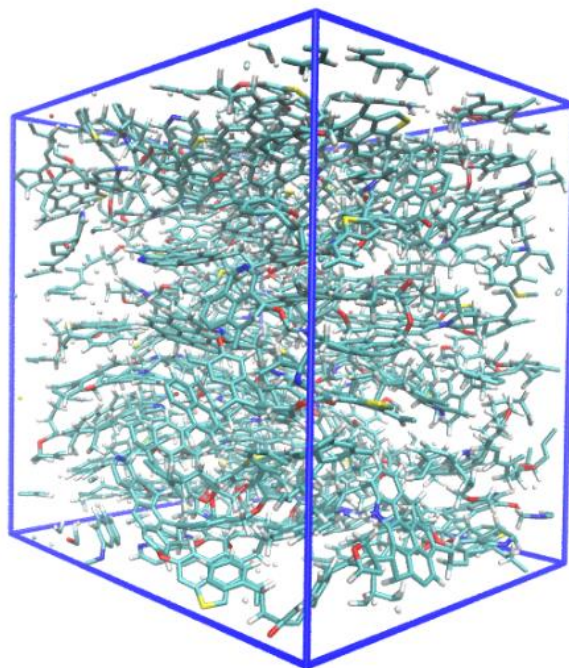


Fig 4.4: Type II Kerogen structure used for simulation

Quartz (SiO_2) molecules were used to build a 4.5 nm pore channel representing the inorganic pores in tight formations. For the organic pore channel, we used carbon nanosheets to build a 5 nm pore channel, to study gas adsorption along the pore walls and interaction mechanism. Fig 4.5 and 4.6 show the initial model setup for methane in a silica (SiO_2) pore channel and ethane in a carbon nanopores channel respectively. The initial models can be found in the supplementary section of this work. Methane, ethane and carbon dioxide were then flow across the different pore channels to determine their degree of adsorption.

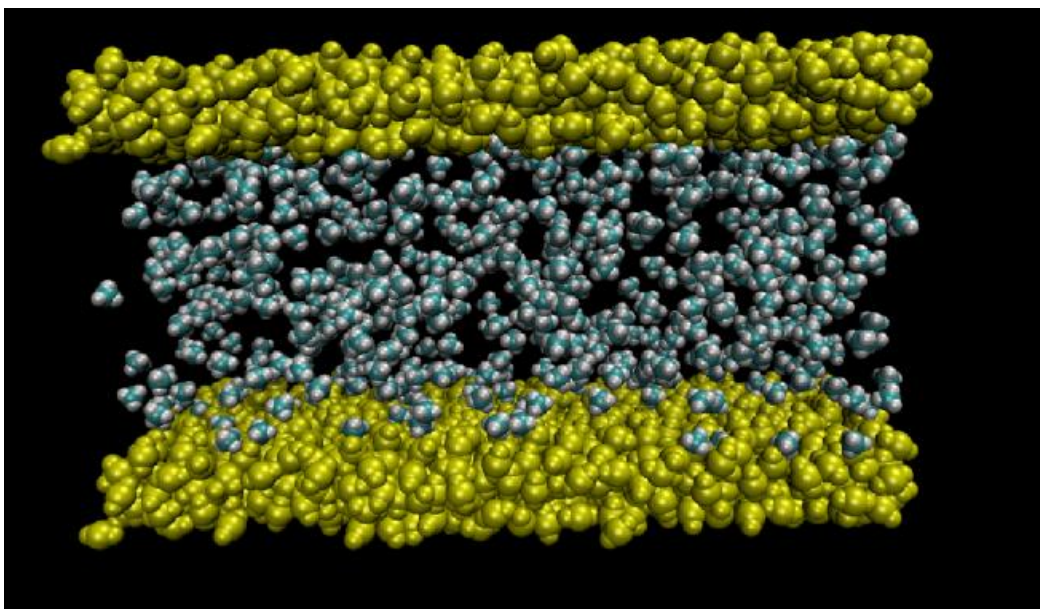


Fig 4.5: Initial model of methane molecules in 4.5nm silica pore channel.

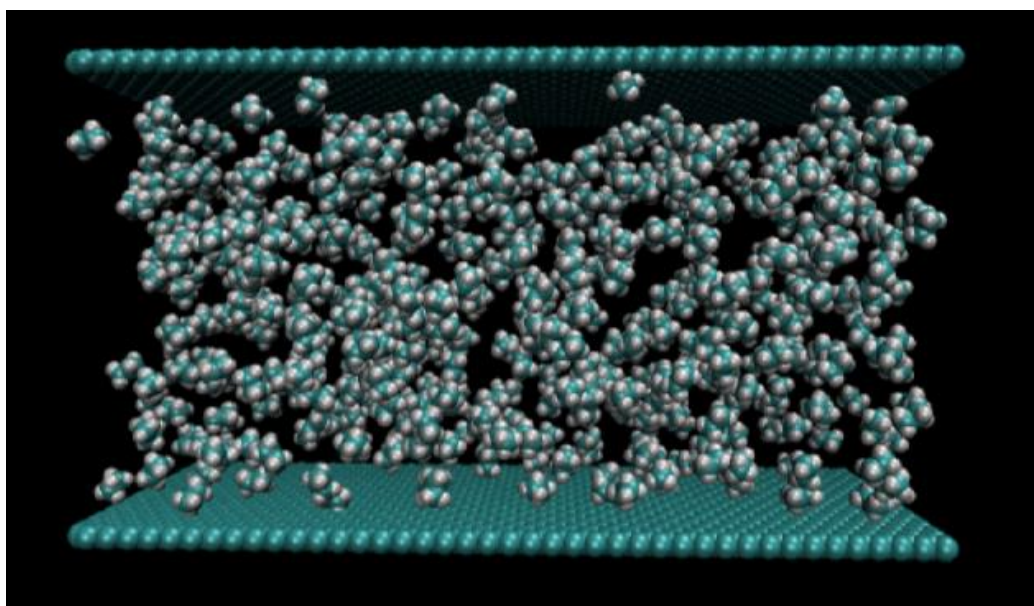


Fig 4.6: Initial model of ethane molecules in a 5 nm carbon channel

In this simulation CH₄, CO₂ and C₂H₆ are modeled using the Trappe force field which was designed for hydrocarbon molecules. In the Trappe force field, the non-bonded interactions between atoms that are separated by more than three bonds or from different molecules are described by the pair wise additive Lennard-Jones (LJ) 12-6 potentials. A cut off distance of 1.4 nm is used for the Van der Waals forces of attraction. Periodic boundary conditions have been applied in all directions.

In our MD simulation, we employed the constant number of particles, constant pressure, and constant temperature ensemble (NPT). For the MC simulations, we used the Grand Canonical Monte Carlo (GCMC) ensemble in which the chemical potentials of the adsorbing fluid, the volume, and the temperature of the system is fixed. The chemical potential can be calculated directly from the reservoir pressure from the equation;

$$\mu = \mu^0 + RT \ln \left(\frac{\varphi^p}{p^0} \right) \quad (3.7)$$

Where μ is the chemical potential, μ^0 and P^0 is the reference chemical potential and pressure respectively. P is the reservoir pressure and φ is the fugacity coefficient. The temperature T and the chemical potential of the adsorbate phase μ , which is assumed to be in equilibrium with a gas reservoir, are fixed. MD will be used to calculate the density of the adsorbed region while GCMC algorithm calculates the adsorption isotherm.

In Monte Carlo simulation run, if the energy difference between the new configuration and the old ($E_{\text{new}} - E_{\text{old}}$) is $\Delta E < 0$ the configuration is accepted. In the case where $\Delta E > 0$, the new configuration is accepted with a Boltzmann-weighted probability of $\exp(-\Delta E/kT)$, where k is the Boltzmann constant and T is temperature of the system (Dubbeldam et al., 2004). There are several moves involved in updating the MC configuration and such are; swap translations and

orientation-biased insertions. A translation move which is giving a particle a random translation is either accepted or rejected based on the difference in energy between the new configuration and the old configuration. For a swap move, a particle is inserted or removed randomly with a 50% probability to allow a chemical equilibrium between an imaginary gas reservoir and your system. The orientation-based insertions are used especially in systems with high density under high pressure to insert particles to favorable conformations in the purpose of increasing the acceptance ratio of the moves. In this work we used the RASPA open source package for MC simulations developed by Dubbeldam et al (2009). For the MD simulations we used the GROMACS 5.3 software. The system is equilibrated with a fixed temperature using the Berendsen thermostat and later on placed in a pressure bath using the Berendsen pressure coupling. For our production run, the temperature coupling is switched to the Nose-Hoover thermostat and pressure coupling to Parrinello-Rahman coupling. A typical MD production run of 5ns was used, and with a time step of 0.001 ps to integrate the equations of motion.

4.2 Results

4.2.1. Adsorption of Methane and CO₂ in Kerogen Nanopores

In this work, we have studied the adsorption capacity of methane and CO₂ in type II kerogen. Methane and CO₂ will turn to be adsorbed differently based on the mineralogy of the pore surface.

In a nanoscale environment which acts as a confinement media the interaction energy between the rock surface and gas is greatly enhanced, which results in a general increase in attraction relative to a free or macro pore environment. From Fig 4.7 (a &b) the total amount of CH₄ and CO₂ increases with increasing pressure as expected and is in agreement with the experimental work by Cao et al (2004), on the study of methane adsorption in carbonaceous materials. Also

there is a slight decrease in methane adsorption capacity at higher pressures due to lesser structured layering on the surface of smaller pores (Sharma et al., 2014). Both CO₂ and methane will turn to be adsorbed in kerogen till it reaches its adsorption equilibrium at higher pressures.

Figures 4.7a and 4.7b compares the adsorption of CO₂ and CH₄ in kerogen at the same conditions. CO₂ shows a much higher adsorption capacity, 1.5 times than that of CH₄, the higher uptake of CO₂ is due to the higher density of CO₂ at those conditions (see Fig 4.9). This clearly shows the viability of CO₂ to be used for enhanced gas recovery and sequestration than methane. Excess adsorption isotherms for CH₄ and CO₂ show an interesting trend (Fig 4.8). As reported by Wu et al (2016), CO₂ and CH₄ excess adsorption capacity initially increases, and then decreases as pressure increases (Fig 4.8). At lower pressure, more methane molecules can be adsorbed in the absence of pore walls; up to pressure where CO₂ approaches super critical state (1,000 – 1,500 psi) which favors more structural arrangement.

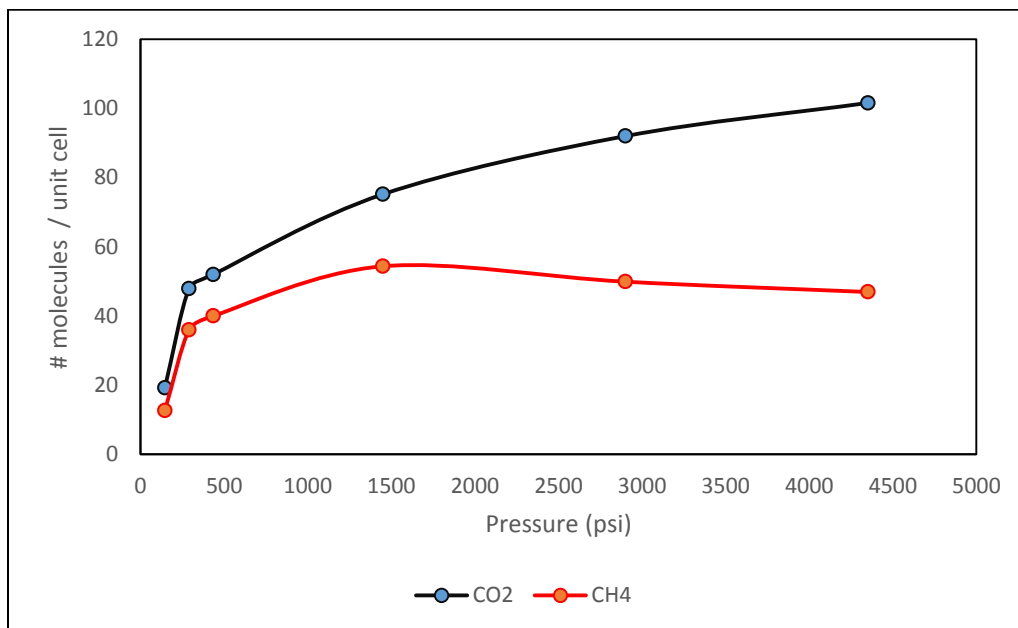


Fig 4.7a: Absolute adsorption of CO₂ and CH₄ in kerogen showing the total number of molecules in a unit cell after simulation.

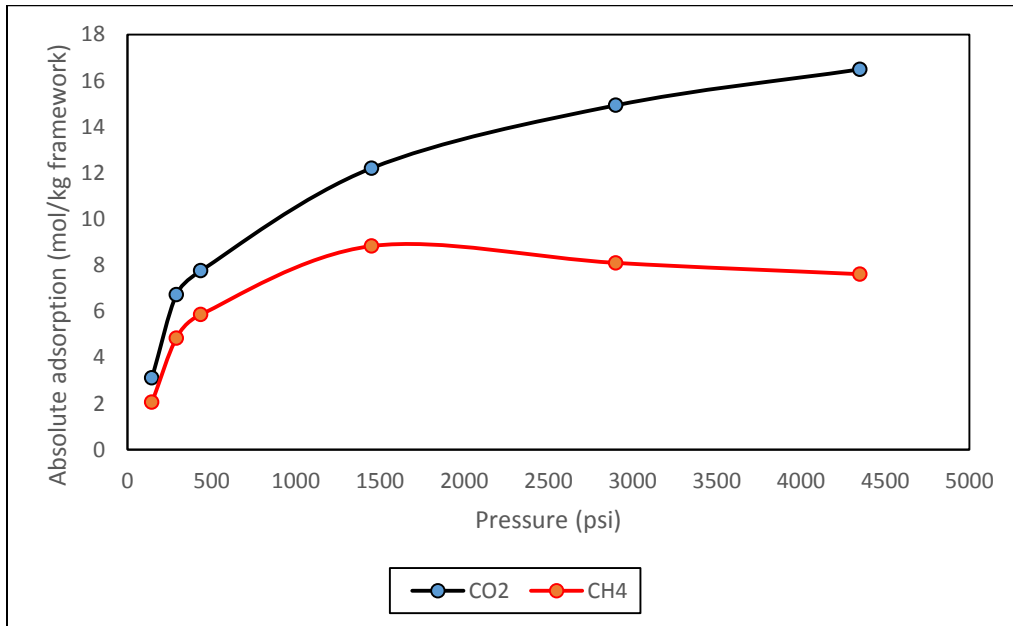


Fig 4.7b: Absolute adsorption of CO₂ and CH₄ in kerogen showing the moles per kilogram for the entire simulation framework.

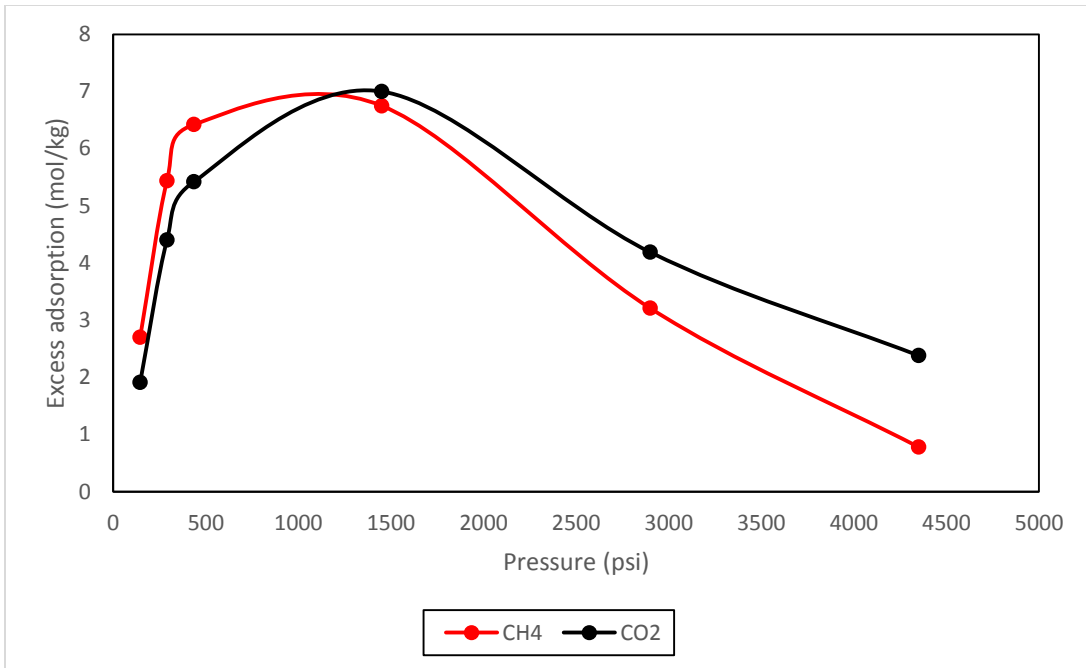


Fig 4.8: Excess adsorption of CO₂ and CH₄ in kerogen

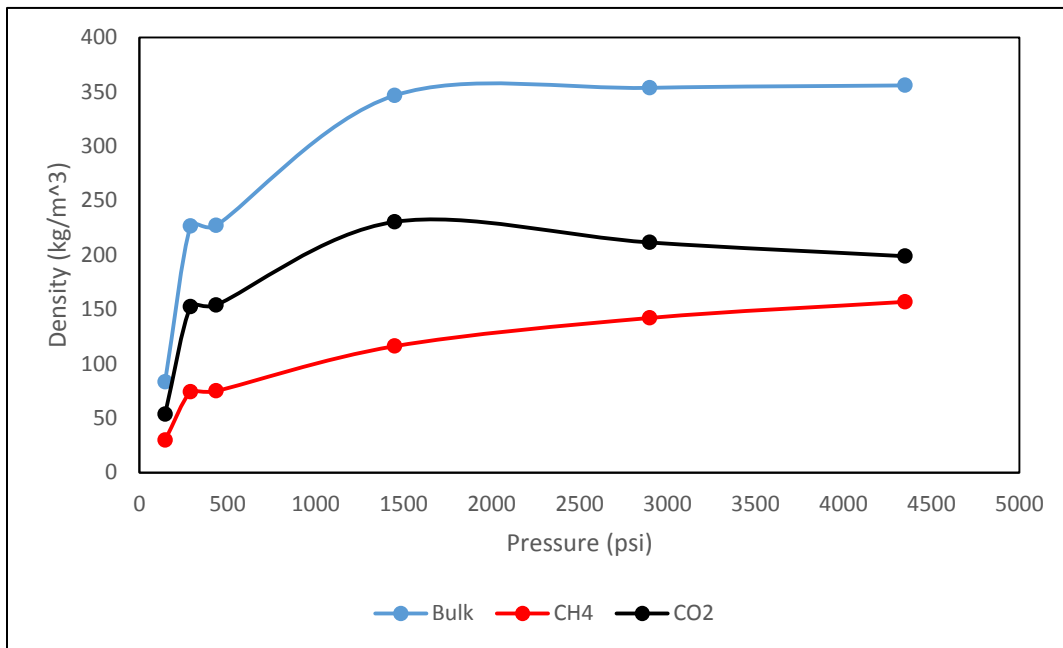


Fig 4.9: Density of adsorbed fluids in kerogen

4.2.2 Adsorption Of Methane, Ethane and CO₂ In Silica and Organic Pore Channel

Looking at the adsorption capacity of CH₄, C₂H₆ and CO₂ in different pore walls and sizes, we simulated both inorganic pore which is comprised of predominantly quartz (silica) and an organic pore which is represented by carbon. In Fig 4.10 (a ,b&c) it is clear that molecules turn to be adsorbed at the pore walls due to very strong fluid-rock interaction. Due to these forces of attraction between the molecules of the fluid and wall, there will be a heterogeneous fluid distribution within the pore channel. Most of the molecules can be seen layered on the surface of the walls.

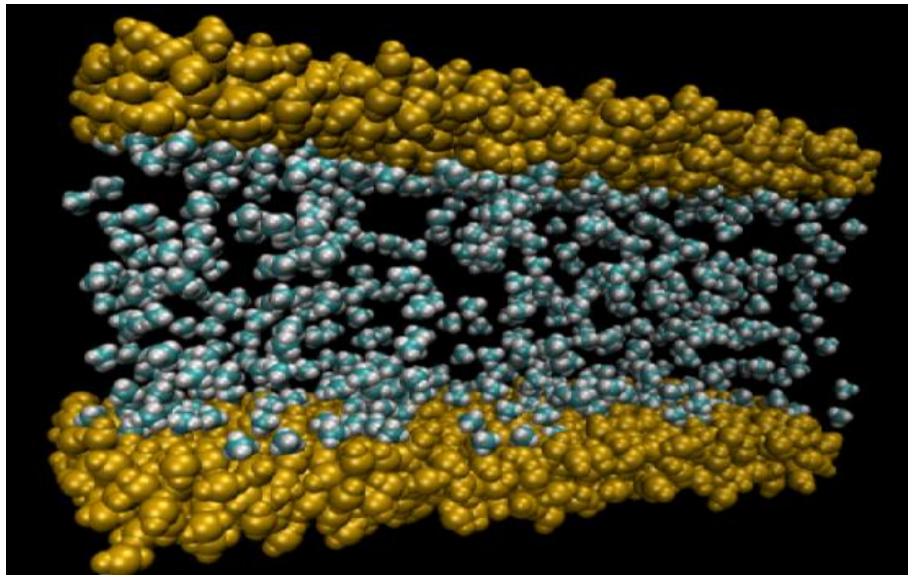


Fig 4.10a: Methane and ethane adsorption in Silica nanopores channel (orange color represents SiO₂ molecules)

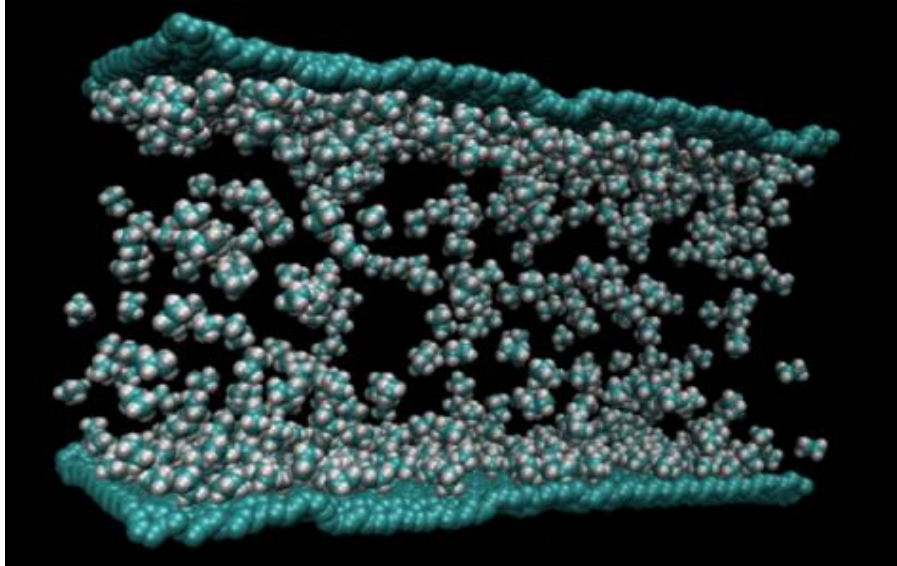


Fig 4.10b: Methane and ethane adsorption in carbon nanopores channel

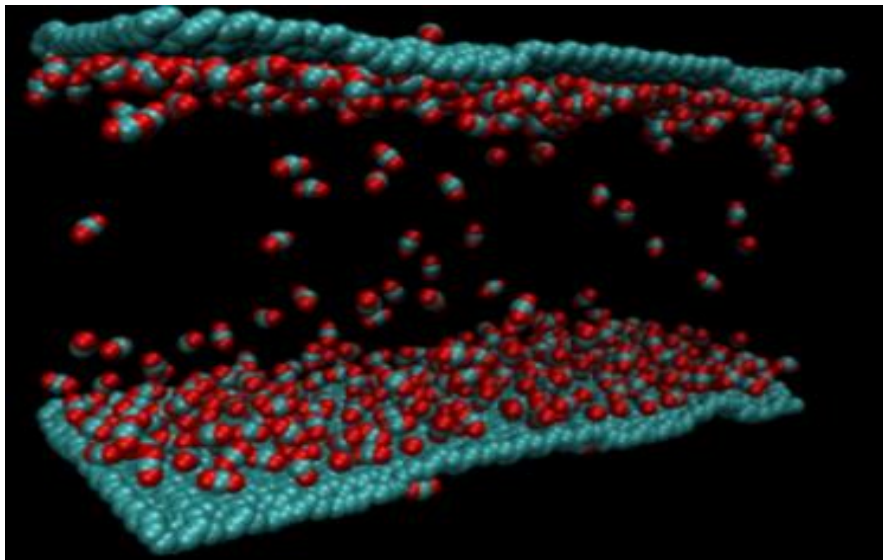


Fig 4.10c: CO₂ adsorption in carbon nanopores channel

CO₂ has the highest adsorption capacity both on inorganic and organic pores as compared to methane and ethane as shown in Fig 4.11 (a & b). Ethane on the other hand has a higher adsorption capacity than methane. The density of molecules at the pore center is

significantly less than at the walls, however, in case where there is increase in pressure; the density at the center will increase due to increased movements of the molecules (Sharma et al., 2016).

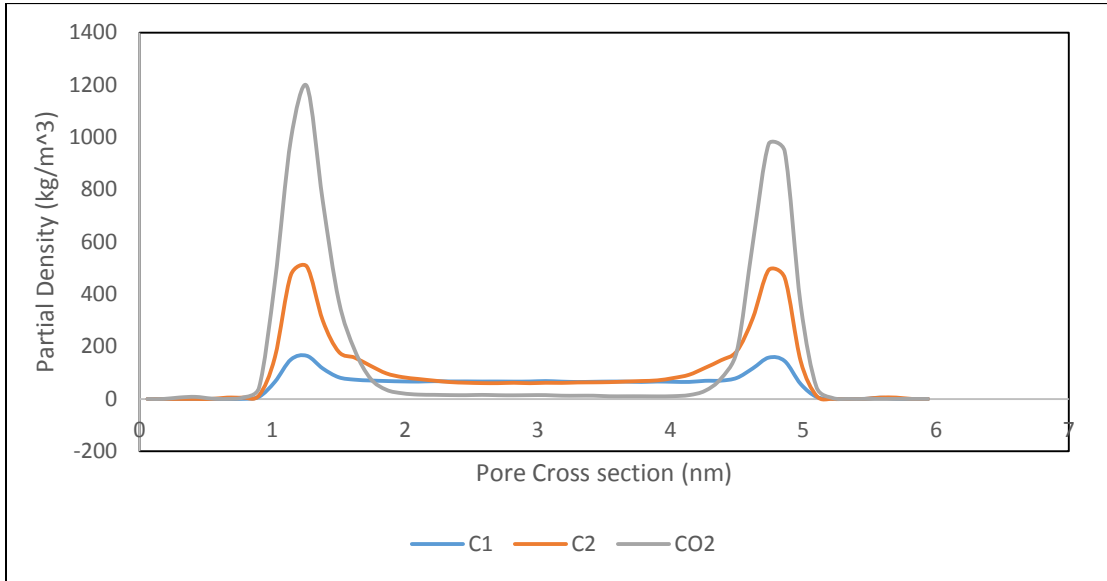


Fig 4.11a: partial density of methane, ethane and CO₂ in silica nanopore

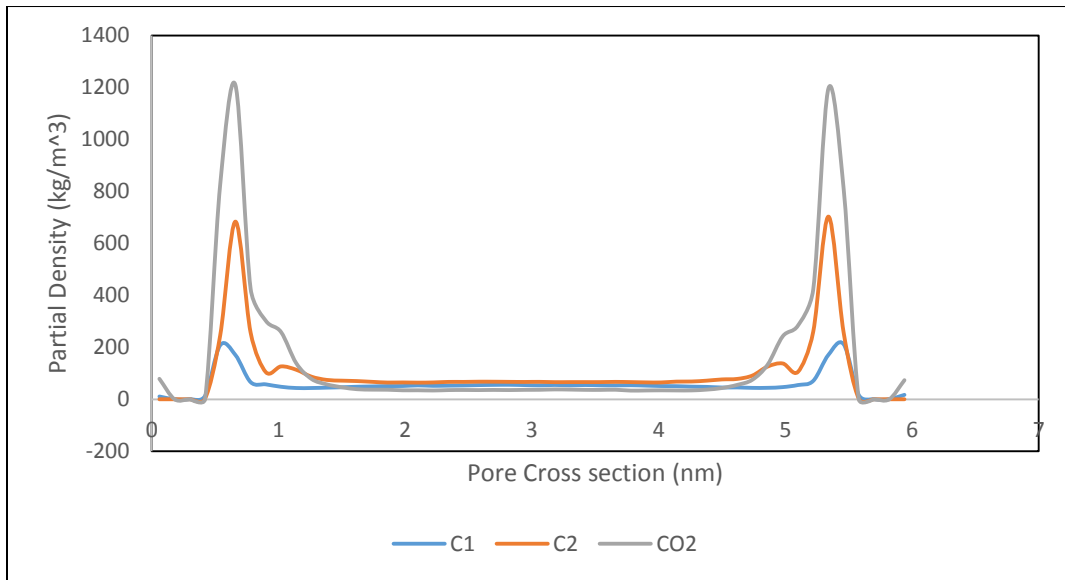


Fig 4.11b: partial density of methane, ethane and CO₂ in carbon nanopores; more CO₂ molecules are adsorbed on the pore wall, followed by ethane and to a lesser extent methane.

4.3. Conclusions

GCMC and NEMD simulations have been performed to study adsorption of methane, ethane and carbon dioxide in kerogen and silica. Our results show that;

- 1) CO₂ has the largest adsorption capacity for both organic and inorganic pores, hence a good candidate for enhanced gas recovery and carbon sequestration in depleted shale gas reservoirs.
- 2) The amount of adsorption is more in organic pores for all studied gases, which implies that shale reservoirs with higher TOC will tend to trap more gases restricting flow and production.
- 3) This work provides a methodological study of shale gas systems which is difficult to isolate properties and study in the lab.
- 4) Creation of a realistic Kerogen model using MD simulations which can be used to study transport properties of gases.

References

A. Sharma, S. Namsani and J. Singh. “Molecular simulation of shale gas adsorption and diffusion in inorganic nanopores”. *Molecular Simulation*, 2016.

B. J. Anderson, J. W. Tester, G. P. Borghi, and B. L. Trout. Properties of inhibitors of methane hydrate formation via molecular dynamics simulations. *J. Am. Chem. Soc.*, 127:17852–17862, 2005.

Bae JS, Bhatia SK. High-pressure adsorption of methane and carbondioxide on coal. *Energy Fuels*. 2006; 20 (6):2599–607.

Berendsen HJC, Vanderspoel D, Vandrunen R. Gromacs: a message-passing parallel molecular-dynamics implementation. *Comput Phys Commun*. 1995; 91(1–3):43–56.

C. H. Sondergeld, R. J. Ambrose, C. S. Rai, and J. Moncrieff, “Micro-structural studies of gas shales,” in *SPE Unconventional Gas Conference*. Society of Petroleum Engineers, 2010.

Cao D, Wu J. Self-diffusion of methane in single-walled carbon nanotubes at sub- and supercritical conditions. *Langmuir*. 2004; 20:3759– 3765.

Dubbeldam D, Calero S, Ellis D, et al. *RASPA 1.0: Molecular Software Package for adsorption and diffusion in nanoporous materials*. Evanston: Northwestern University; 2008.

Dubbeldam D, Calero S, Vlugt TJH, et al. United atom force field for alkanes in nanoporous materials. *J Phys Chem B*. 2004b; 108 (33):12301–13.

Espitalie, J., Deroo, G., Marquis, F., 1985. *Rock-Eval pyrolysis and its applications*. Rev. Inst. Francais Du Pet. 40, 563–579.

Gerhard, L.C., Anderson, S.B., Fischer, D.W., 1990. *Petroleum geology of the Williston Basin*. AAPG Mem. 51, 507–559.

Hackley, P.C., Araujo, C.V., Borrego, A.G., Bouzinos, A., Cardott, B.J., Cook, A.C., Eble, C., Flores, D., Gentzis, T., Gonçalves, P.A., 2015. *Standardization of reflectance measurements in dispersed organic matter: results of an exercise to improve inter laboratory agreement*. Mar. Pet. Geol. 59, 22–34

K. Wu, Z. Chen, X. Li, X. Dong “Methane storage in nanoporous material at supercritical temperature over a wide range of pressures” Sci Rep-UK, 6 (2016), p. 33461.

Khatibi, S., Ostadhassan, M., Tuschel, D., Gentzis, T., Bubach, B. and Carvajal-Ortiz, H., (2017) *Raman spectroscopy to study thermal maturity and elastic modulus of Kerogen*, International Journal of Coal Geology.

Kuhn, P., Di Primio, R., Horsfield, B., 2010. *Bulk Composition and Phase Behaviour of Petroleum Sourced by the Bakken Formation of the Williston Basin*, Geological Society. Petroleum Geology Conference series. Geological Society of London, London, pp. 1065–1077.

Kumar, V., Sondergeld, C.H., Rai, C.S., 2012. *Nano to macro mechanical characterization of shale*. In: SPE Annual Technical Conference and Exhibition. Society of Petroleum Engineers

LeFever, J.A., Martiniuk, C.D., Dancsok, E.F., Mahnic, P.A., 1991. *Petroleum potential of the middle member, Bakken Formation, Williston Basin*. In: Williston Basin Symposium.

Li, C., Ostadhassan, M., Kong, L., 2017. *Nanochemo-mechanical Characterization of Organic Shale Through AFM and EDS*, SEG Technical Program Expanded Abstracts 2017. Society of Exploration Geophysicists, pp. 3837–3840.

Liang Huang, Zhengfu Ning, Qing Wang, Rongrong Qi, Yan Zeng, Huibo Qin, Hongtao Ye, Wentong Zhang “Molecular simulation of adsorption behaviors of methane, carbon dioxide and their mixtures on kerogen: Effect of kerogen maturity and moisture content” , *Fuel*, Volume 211, 2018, Pages 159-172.

Liu, K., & Ostadhassan, M. (2017). *Multi-scale fractal analysis of pores in shale rocks*. *Journal of Applied Geophysics*, 140, 1-10.

Liu, K., & Ostadhassan, M. (2017). *Quantification of the microstructures of Bakken shale reservoirs using multi-fractal and lacunarity analysis*. *Journal of Natural Gas Science and Engineering*, 39, 62-71.

Liu, K., Ostadhassan, M., & Kong, L. (2017). *Pore Structure Heterogeneity in Middle Bakken Formation*. Paper presented at the 51st US Rock Mechanics/Geomechanics Symposium.

Liu, K., Ostadhassan, M., 2017. *Microstructural and geomechanical analysis of Bakken shale at nanoscale*. *J. Pet. Sci. Eng.* 153, 133–144.

Liu, K., Ostadhassan, M., Gentzis, T., Carvajal-Ortiz, H., Bubach, B., 2017. *Characterization of geochemical properties and microstructures of the Bakken Shale in North Dakota*. *Int. J. Coal Geol.*

Liu, K., Ostadhassan, M., Zhou, J., Gentzis, T., & Rezaee, R. (2017). *Nanoscale pore structure characterization of the Bakken shale in the USA*. *Fuel*, 209, 567-578.

Lu M, Connell LD, Pan ZJ. A model for the flow of gas mixtures in adsorption dominated dual-porosity reservoirs incorporating multi-component matrix diffusion-Part II numerical algorithm and application examples. *J Petrol Sci Eng.* 2008; 62(3–4):93–101.

M. E. Curtis, R. J. Ambrose, C. H. Sondengeld, and C. S. Rai, “Structural characterization of gas shales on the micro- and nanoscales,” in *Canadian Unconventional Resources & International Petroleum Conference*. Society of Petroleum Engineers, 2010.

M. Kazemi, and A.T Borujeni “Effect of Adsorption in flow of Gases in Organic Nanopores: A Molecular Dynamics Study. *Unconventional Resources Technology Conference*, 2016, Texas, USA.

P. Ungerer, J. Collell, and M. Yiannourakou, “Molecular modeling of the volumetric and thermodynamic properties of kerogen: Influence of organic type and maturity,” *Energy and Fuels*, vol. 29, pp. 91–105, 2015.

Peng D, Robinson DB. New 2-constant equation of state. *Ind Eng Chem Fund.* 1976;15(1):59–64.

Smith, M.G., Bustin, R.M., 1995. *Sedimentology of the Late Devonian and Early Mississippian Bakken Formation, Williston Basin*. In: *Williston Basin Symposium*.

Smith, M.G., Bustin, R.M., 2000. *Late Devonian and Early Mississippian Bakken and Exshaw black shale source rocks, Western Canada Sedimentary Basin: a sequence stratigraphic interpretation*. *AAPG Bull.* 84, 940–960.

Zhang, Junfang & Liu, Keyu & Clennell, Michael & Dewhurst, David & Pan, Zhejun & Pervukhina, Marina & Han, Tongcheng. (2015). Molecular simulation studies of hydrocarbon and carbon dioxide adsorption on coal. *Petroleum Science*. 12. 10.1007/s12182-015-0052-7.